

# Adapting protein language models for structure-conditioned design

Jeffrey A. Ruffolo<sup>1,†</sup>, Aadyot Bhatnagar<sup>1</sup>, Joel Beazer<sup>1</sup>, Stephen Nayfach<sup>1</sup>, Jordan Russ<sup>1</sup>, Emily Hill<sup>1</sup>, Riffat Hussain<sup>1</sup>, Joseph Gallagher<sup>1</sup>, and Ali Madani<sup>1,†</sup>

<sup>1</sup> Profluent Bio, Berkeley, CA, USA

1 Generative models for protein design trained on experimentally determined structures have proven useful for a variety of design tasks.  
2 However, such methods are limited by the quantity and diversity of structures used for training, which represent a small, biased fraction  
3 of protein space. Here, we describe proseLM, a method for protein sequence design based on adaptation of protein language models to  
4 incorporate structural and functional context. We show that proseLM benefits from the scaling trends of underlying language models, and that  
5 the addition of non-protein context – nucleic acids, ligands, and ions – improves recovery of native residues during design by 4-5% across  
6 model scales. These improvements are most pronounced for residues that directly interface with non-protein context, which are faithfully  
7 recovered at rates >70% by the most capable proseLM models. We experimentally validated proseLM by optimizing the editing efficiency of  
8 genome editors in human cells, achieving a 50% increase in base editing activity, and by redesigning therapeutic antibodies, resulting in a  
9 PD-1 binder with 2.2 nM affinity.

protein design | large language models | genome editing | antibody design

## 1 Introduction

2 Protein sequence design aims to identify an amino acid sequence that will fold into a desired backbone and  
3 carry out a function of interest. The ability to design proteins with novel functions has broad applications  
4 in biotechnology and medicine, including the development of therapeutics, vaccines, and industrial enzymes.  
5 Physics-based methods, such as Rosetta (1), approach protein design as an optimization problem, searching  
6 for sequences that minimize an energy function. However, these methods are limited by the accuracy of  
7 the underlying energy function and are computationally expensive in practice. Recently, deep learning  
8 approaches, which learn a mapping from structure to sequence, have emerged as an alternative to physics-  
9 based methods (2-4). Generative models for protein design, such as ProteinMPNN (3), have proven  
10 successful across a variety of tasks, including design of protein binders (3), assemblies (5), diversified  
11 enzymes (6), and conformational switches (7). Despite their success, protein design models trained solely on  
12 experimentally determined structures are ultimately limited by the quantity and diversity of their training  
13 data. While the Protein Data Bank (PDB) (8) contains over 200,000 protein structures, this number is  
14 dwarfed by the number of sequences identified through genomic and metagenomic sequencing efforts. To  
15 overcome this disparity, predictions from AlphaFold2 (9) have been used to supplement the structures used  
16 for training (4). This approach has been shown to improve the performance of protein design models (4),  
17 but is still limited by the number of structures that can be predicted and the accuracy of the predictions.

18 Protein language models present an alternative means of modeling protein sequence-function relationships.  
19 These models learn directly from sequences through self-supervised training objectives, such as masked  
20 residue prediction and next-residue prediction. With increasing numbers of parameters, protein language  
21 models have been shown to capture properties including structure (10, 11) and function (12, 13). Design  
22 with protein language models is largely a challenge of steering generation towards a desired region of  
23 sequence space. Steering of generated sequences is typically achieved through fine-tuning on curated datasets  
24 of family- or function-specific proteins. This approach has proven successful for a variety of enzyme families,  
25 including lysozymes (14), carbonic anhydrases, lactate dehydrogenases (15), and complex genome editing

†To whom correspondence should be addressed. E-mail: jeff@profluent.bio, ali@profluent.bio

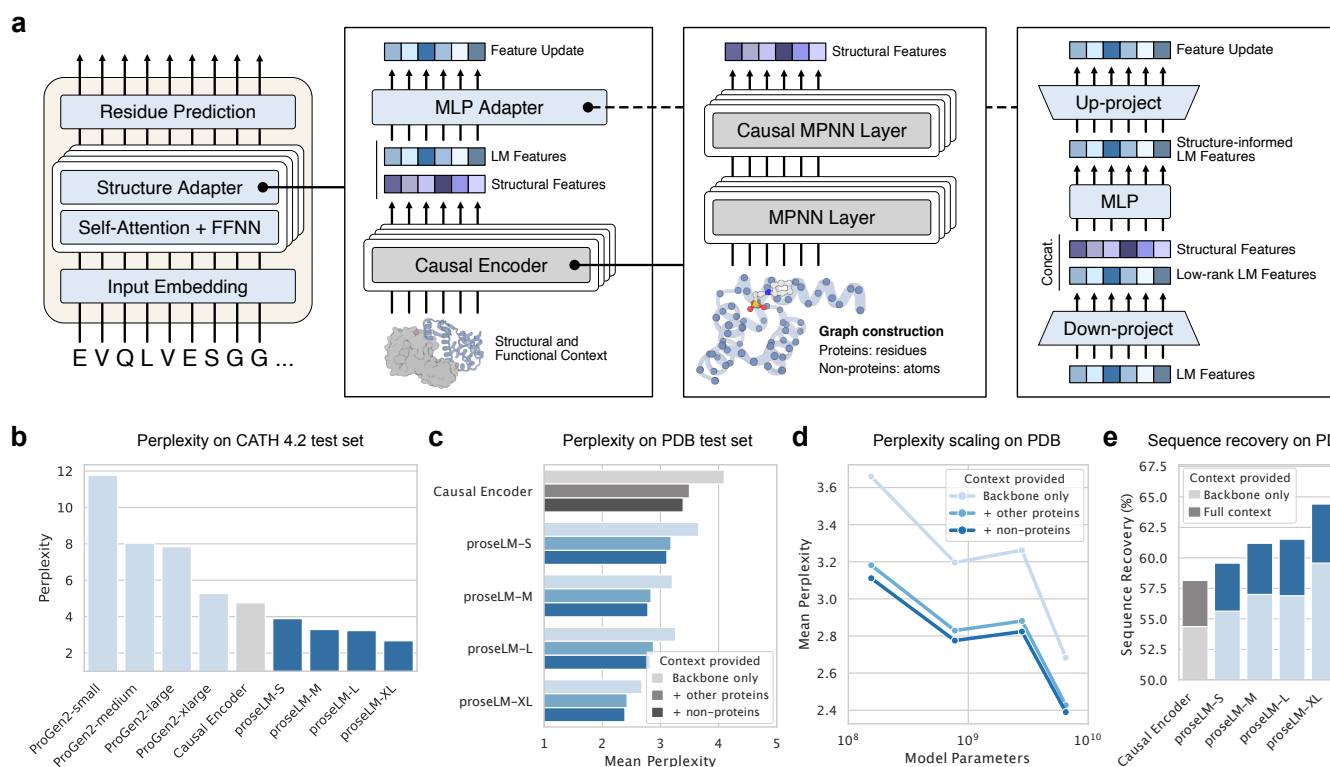


**Figure 1. Design of protein sequences for diverse backbones.** (a) Diagram of proseLM architecture. Structural adapter layers are placed after each layer of the pre-trained language model. In each adapter layer, structural context from the causal encoder is combined with language model embeddings to condition sequence generation. (b) Perplexity of ProGen2 pre-trained language models and single-chain proseLM models on the CATH 4.2 test set collected by Ingraham et al. (2). (c) Perplexity of proseLM models on the clustered PDB dataset collected by Dauparas et al. (3). Perplexity is reported as the mean of cluster-averaged values. For all models, perplexity decreases as additional structural and functional context is provided. (d) Perplexity with respect to total model parameters for proseLM models trained on the PDB with increasing levels of structural and functional context provided. (e) Native sequence recovery for fully designed sequences from proseLM models. Sequence recovery is reported as the median of cluster-averaged values. For all models, native sequence recovery increases when structural and functional context is provided.

systems (16). However, the dependence on natural examples for fine-tuning currently limits the scope of design with protein language models to known protein families and functions. Further, it does not offer a straightforward means of incorporating precise atomistic information into the design process, instead relying on the model to implicitly learn these constraints from the fine-tuning data.

In this work, we describe proseLM (protein structure-encoded language model), a method for steering protein language models for design tasks by providing explicit structural and functional information. ProseLM leverages parameter-efficient adaptation of protein language models to incorporate structural and functional information, including the backbone-of-interest and nearby context (proteins, nucleic acids, ligands, ions, etc.). ProseLM effectively incorporates this context while benefiting from the scaling trends of the underlying language models, enabling high rates of native sequence recovery. We experimentally validate proseLM by designing functionally improved genome editors and therapeutic antibodies.

## Results

**Protein structure-encoded language model.** Our method for protein sequence design, proseLM, leverages pre-trained protein language models for structure-conditioned design. We take the ProGen2 language models (13) as a foundation and propose a conditional adapter for parameter-efficient incorporation of structural and functional context.

Several methods have been proposed for parameter-efficient fine-tuning of large language models (17–19), enabling specialization of models by training a small fraction of the total parameters. In this work, we build

44 on adapters, which introduce a set of bottlenecked operations that modify the outputs of each model layer.  
45 For proseLM, we follow Houlsby et al (18) and introduce adapter layers that update the outputs of the  
46 simultaneous attention and feed-forward operations of each ProGen2 layer (Figure 1A). With sufficiently  
47 reduced bottleneck dimension, the number of parameters in these adapter layers are minuscule with respect  
48 to the pre-trained model. To inject structural information into the ProGen2 language models, we propose  
49 an adapter architecture that conditions in the low-rank representation using a multi-layer perceptron  
50 (MLP). In this way, the adapter layers maintain parameter efficiency while incorporating structural context  
51 throughout the depth of the language model.

52 Structural context for conditioning is obtained from a pre-trained causal encoder, which is trained in a  
53 similar fashion to prior encoder-decoder protein design models. The causal encoder architecture consists of  
54 alternating message-passing (MPNN) and invariant-point message-passing (IPMP) (20) encoder layers (eight  
55 total) followed causally masked MPNN and IPMP layers (four total). IPMP layers modify standard MPNN  
56 layers by adding frame-based inter-residue features, and have been proposed as a drop-in replacement for  
57 protein side-chain modeling and sequence design (20). Following ProteinMPNN, the causal encoder is  
58 trained to decode randomly permuted sequences given a fixed backbone (3). Different from the natural  
59 N-to-C fixed decoding order, this formulation enables conditioning on later residues for design tasks where  
60 some of the sequence should remain constant. We additionally train the causal encoder with masked  
61 structural spans, following the span sampling scheme used for ESM-IF1 (4). When trained on the CATH  
62 4.2 dataset (2, 21), the causal encoder achieves a median sequence recovery of 47.24% and perplexity of  
63 4.76 (Table S1) on the test set. Taken together, this performance is similar to ProteinMPNN (trained  
64 without noise) (3), which achieves a median sequence recovery of 45.96% and perplexity of 4.61 on the same  
65 proteins (22).

66 To implement proseLM, we combined the pre-trained causal encoder with pre-trained ProGen2 language  
67 models (13) using parameter-efficient adapter layers. Standard adapter layers are typically composed of a  
68 feed-forward network with a bottleneck dimension, expressed as (18):

$$69 \quad \mathbf{h} \leftarrow \mathbf{h} + f(\mathbf{h} \mathbf{W}_{\text{down}}) \mathbf{W}_{\text{up}} \quad [1]$$

70 where  $h$  is the language model embeddings,  $f$  is a non-linear activation function (typically ReLU), and  
71  $W_{\text{down}}$  and  $W_{\text{up}}$  are weight matrices for the down- and up-projections, respectively. For proseLM, we  
72 propose a conditional adapter architecture that incorporates structural context into the language model  
73 embeddings using an MLP. The conditional adapter layers are expressed as:

$$74 \quad \mathbf{h}_{\text{LM}} \leftarrow \mathbf{h}_{\text{LM}} + \text{MLP}(\text{Concat}(\mathbf{h}_{\text{LM}} \mathbf{W}_{\text{down}}, \mathbf{h}_{\text{CE}})) \mathbf{W}_{\text{up}} \quad [2]$$

75 where  $h_{\text{LM}}$  and  $h_{\text{CE}}$  are the language model and causal encoder embeddings, respectively. The causal encoder  
76 embeddings are taken from the last decoder layer, just prior to amino acid prediction. By concatenating  
77 the causal encoder embeddings with the low-rank language model embeddings, the conditional adapter  
78 maintains the parameter-efficiency of standard adapters while incorporating conditioning information.  
79 Conditional adapter layers are placed after each of the simultaneous attention and feed-forward layers of  
80 ProGen2, with separately trained weights for each adapter layer. During training, the parameters of the  
81 causal encoder and conditional adapter layers are updated, while the parameters of the language model are  
82 frozen.

83 To test the effectiveness of the conditional adapters for structure-conditioned sequence modeling, we  
84 compared the perplexity of proseLM models trained on the CATH 4.2 dataset to their constitutive models.  
85 For ProGen2 models, perplexity scaled with model size, with ProGen2-xlarge (6.4B parameters) approaching  
86 the performance of the structure-aware causal encoder (Figure 1b). For proseLM models, perplexity further  
87 improved over the causal encoder, following the same scaling trend as the underlying language models. We  
88 next compared the native sequence recovery of proseLM models to the causal encoder. Native sequence  
89 recovery is defined as the percentage of designed residues that match the native sequence for a particular  
90 structure. Native sequence recovery increased with proseLM model scale, with proseLM-XL achieving

91 a 3.59% higher median recovery rate than the causal encoder (Figure S2a). This increase in sequence  
92 discovery was distributed across surface and core residues (Figure S2b) and was most dramatic for larger  
93 proteins (Figure S2c).

94 Training structure-conditioned sequence design methods with Gaussian noise applied to the coordinates  
95 has been shown to increase robustness of single-sequence AlphaFold2 predictions, which can serve as a  
96 proxy for design quality (3). To assess the impact of training with coordinate noise on proseLM, we trained  
97 an additional set of causal encoder and proseLM models with 0.1 Å Gaussian noise added to the backbone  
98 coordinates. As reported for ProteinMPNN, we found that all proseLM models trained with coordinate  
99 noise achieved higher rates of single-sequence prediction structure prediction success with AlphaFold2 (9)  
100 and yielded more confident structures (Figure S3). Interestingly, these improvements were most pronounced  
101 for the causal encoder and smaller proseLM models, suggesting that the larger models are more robust to  
102 structural noise.

103 **Functional context constrains design space.** Protein function depends on interactions with other molecules,  
104 ranging from recognition of specific DNA sequences to coordination of metal ions. While historically these  
105 interactions have been modeled through physics-based methods (1), they have largely been neglected in  
106 recent protein sequence design models. For proseLM, we sought to incorporate functional context beyond the  
107 backbone to include not only protein-protein interactions, but also interactions with arbitrary non-protein  
108 molecules (e.g., nucleic acids, ligands, ions, etc.). We started by extending the causal encoder to consider  
109 protein complexes, which was achieved by simply expanding the existing protein graph to include multiple  
110 chains.

111 Non-protein context is represented as an atomistic graph, with each atom represented as a node with  
112 an associated reference frame. Each atomic frame is constructed using the atom-of-interest and its two  
113 nearest neighbors (Figure S1b). Nodes are initialized with the types of each atom encoded as node features,  
114 along with the distances between the central atom and its neighbors. To incorporate information from  
115 the non-protein context graph into the causal encoder, we introduced an IPMP layer for updating the  
116 atomistic features, followed by a cross-graph IPMP layer for updating the protein residue features. The  
117 cross-graph IPMP layer is similar to the standard IPMP layer, but uses a different set of weights for protein  
118 and atomistic nodes, and does not update the atomistic features. The context-aware causal encoder and  
119 corresponding proseLM models were trained on the multi-chain dataset used for ProteinMPNN (3) in the  
120 same fashion as the single-chain versions, except the causal encoder parameters were frozen during proseLM  
121 training to reduce memory requirements.

122 We first evaluated proseLM on the subset of the PDB test set that contained protein complexes and  
123 interactions with some non-protein entity (Table S3). For each protein chain, we computed the perplexity  
124 given increasing levels of context: backbone only, with other protein chains, and with full context. In  
125 each scenario, perplexity decreased as more context was provided (Figure 1c). This trend held across  
126 model scales, suggesting that even the largest language models benefit from explicit functional information  
127 (Figure 1d). We next evaluated the capabilities of proseLM for design on the test set structures that had  
128 any protein or non-protein interactions. We computed the median native sequence recovery for designs  
129 with proseLM when given the backbone only or full context. Increases in sequence recovery from scaling  
130 models and providing functional context were largely additive, with proseLM models achieving a consistent  
131 4-5% increase in sequence recovery with full context (Figure 1e).

132 The most significant increases in native sequence recovery were for residues within 5 Å of nucleic  
133 acids, ligands, and ions (Figure 2a). The causal encoder, which is the most directly comparable to  
134 recently developed models (23, 24) for context-aware protein sequence design, achieves sequence recovery  
135 (with/without context) of 44.44%/54.90%, 50.00%/64.00%, and 46.15%/66.67% for residues near nucleic  
136 acids, ligands, and ions, respectively. These results are similar to those reported for CARBonAra (24) and  
137 LigandMPNN (23).

138 With the addition of language model components, proseLM models achieve further increases in native  
139 sequence recovery in the vicinity of functional context (Table S3). For ligand and ion interactions, these

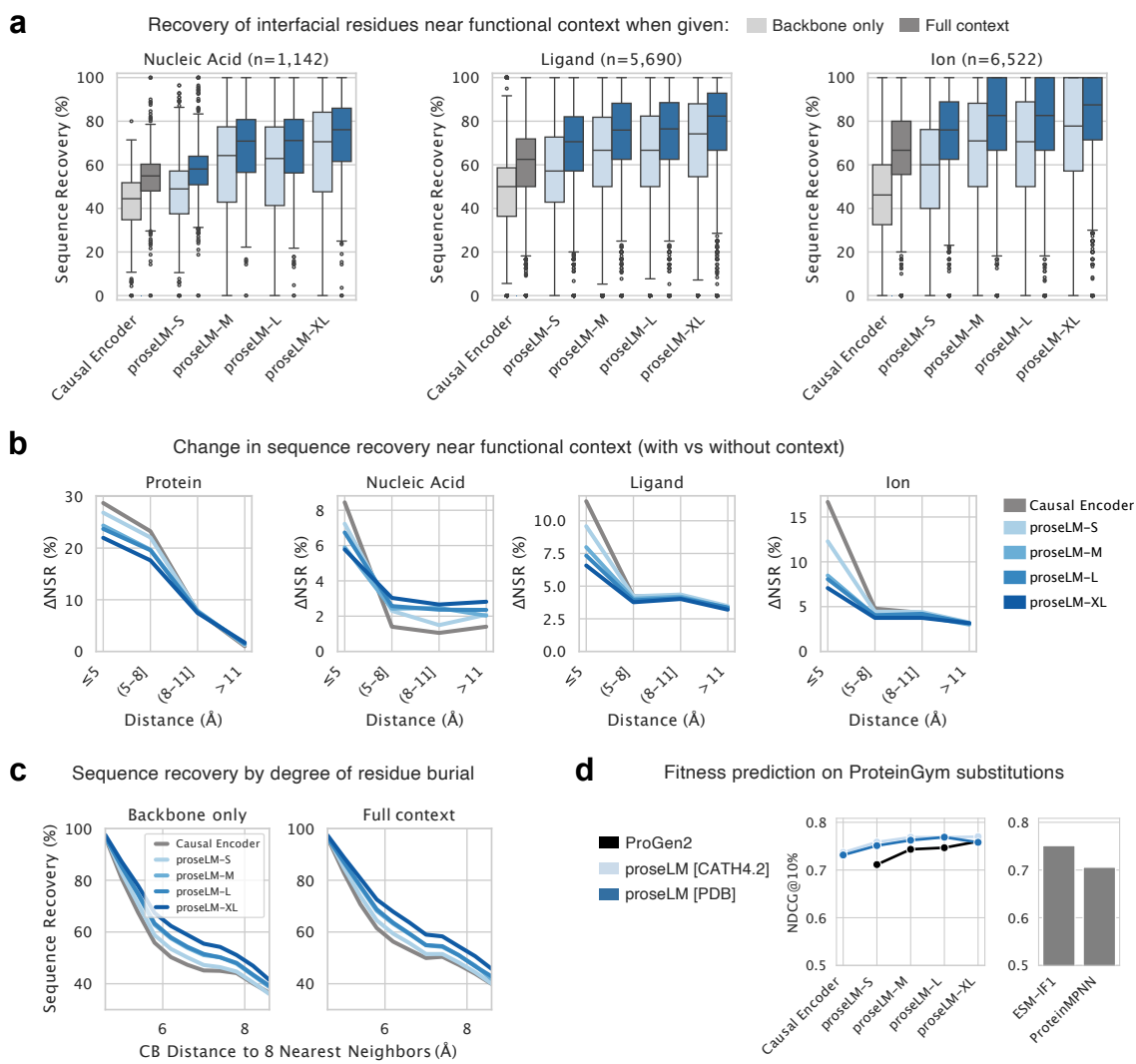


**Figure 2. Modeling protein functional context and fitness.** (a) Median native sequence recovery for residues near nucleic acids, small-molecule ligands, and ions. (b) Change in native sequence recovery with and without structural and functional context as a function of distance from provided context. Smaller models show the largest increases in recovery near the provided context, while all models converge towards lower overall increases in recovery as distance increases. (c) Sequence recovery as a function of residue burial for protein complex targets. When designed with backbone only (single chain) or with protein context, recovery is largely determined by degree of burial. (d) Evaluation of fitness prediction, measured as normalized discounted cumulative gain, for proseLM models. Overall performance is averaged over landscape categories: stability, binding, activity, expression, and organismal fitness.

increases were mostly localized to residues within 5 Å of the provided context (Figure 2b). For nucleic acid interactions, smaller models showed the largest increases in sequence recovery near the provided context, while larger models showed more consistent improvements at greater distances. This suggests that while smaller models benefit from the direct influence of nucleic acid context for local sequence recovery, larger models may be leveraging evolutionary information from pre-training to improve sequence recovery at greater distances. For protein-protein interactions, the effects of context were observable up to 11 Å away, largely due to changes in burial of residues across the designed protein chains (Figure 2c).

**Structure improves modeling of protein fitness.** Protein language models trained on evolutionarily diverse sequences are strong zero-shot predictors (i.e., without labeled data) of protein function, with performance on some landscapes benefiting from increased model scale (12, 13, 25). To investigate the impact of structural conditioning on language model fitness prediction, we evaluated proseLM models on a set of

151 201 deep mutational scan (DMS) datasets curated for ProteinGym (25). We limited our analysis to  
152 datasets where the protein sequence length was less than 1024 residues, which was the context length  
153 used for training ProGen2 models. Log likelihoods were computed for proseLM models trained on the  
154 CATH 4.2 (backbone-only) and PDB (full context) datasets using AlphaFold2-predicted (9) structures from  
155 ProteinGym. Datasets are coarsely categorized as stability, binding, activity, expression, or organismal  
156 fitness, according to the property measured. Following ProteinGym, we report an overall performance as  
157 the average of performance over each category to avoid emphasizing imbalances in the number of datasets  
158 available for each fitness type. We additionally report performance for two recent methods – ESM-IF1 (4)  
159 and ProteinMPNN (3) – to contextualize the performance of proseLM models.

160 We quantify fitness prediction performance according to the normalized discounted cumulative gain  
161 (NDCG) at ten percent (Figure S5) and the Spearman's rank correlation coefficient (Figure S6). Although  
162 Spearman values are more commonly reported for performance across entire fitness landscapes, the NDCG  
163 metric, which focuses on a model's ability to prioritize the highest-fitness sequences, is more aligned with  
164 practical protein engineering settings. Overall, proseLM models achieve higher NDCG values than the  
165 causal encoder and ProGen2 models (Figure 2d). Interestingly, the largest improvements in NDCG are  
166 for smaller language models, while larger proseLM models often performed comparable to the underlying  
167 ProGen2 models. This suggests that larger models gain less new information from structural context,  
168 consistent with prior work showing that larger protein language models build increasingly accurate internal  
169 representations of structure (11).

170 For stability landscapes, we observed opposing trends between structure-conditioned and standard  
171 language models. The causal encoder was a better predictor of high-stability proteins, while proseLM  
172 models showed degraded performance with increased scale. For binding-related fitness landscapes, proseLM  
173 models outperformed the causal encoder and underlying ProGen2 models. Interestingly, the backbone-only  
174 proseLM models trained on the CATH 4.2 dataset consistently outperformed those trained on the full PDB  
175 with additional context. This discrepancy highlights a tradeoff between models that learn to implicitly  
176 model functional context and those that explicitly incorporate given context. While the proseLM models  
177 trained on the PDB are able to effectively leverage binding partners for prediction, they appear less capable  
178 of inferring binding from protein structure alone.

179 **Experimental validation of functional protein design.** Given the compelling performance of proseLM on *in*  
180 *silico* protein design and fitness prediction tasks, we next sought to test its practical utility for functional  
181 protein design. Towards this goal, we focused on structure- and function-guided optimization of two broadly  
182 relevant protein systems: genome editors and antibodies.

183 **Genome editor design.** Genome editing technologies repurposed from bacterial anti-phage defense systems  
184 have revolutionized life science research and are being actively developed for agricultural and therapeutic  
185 applications. In particular, the Cas9 protein from *Streptococcus pyogenes* (SpCas9) has formed the foundation  
186 of several downstream editing technologies, including the targeted editing of base pairs in the genome (26).  
187 As an RNA-guided endonuclease, the functional activity of SpCas9 is highly dependent on interactions  
188 with its guide RNA and the target DNA. We reasoned that the incorporation of structural and functional  
189 context into protein language models could enable the local optimization of SpCas9 for increased activity in  
190 human cells.

191 To design variants of SpCas9 with proseLM while maintaining functional activity, we utilized a multi-state  
192 conditioning strategy (Figure 3a) that included both the binary and catalytic states of the protein in  
193 complex with guide RNA (and DNA for catalytic state). We additionally found it helpful to incorporate  
194 evolutionary and functional information in the form of residue-wise conservation patterns from aligned  
195 natural sequences and experimental mutation-scanning data, respectively. When combined with multi-state  
196 conditioning, this design strategy enabled sampling of low-perplexity sequences within 200 mutations of the  
197 wild type sequence (Figure S7). We selected a set of seven designs to test for genome editing in HEK293T  
198 cells via co-transfection of the designed proteins and single-guide RNAs (sgRNA) targeting one of three

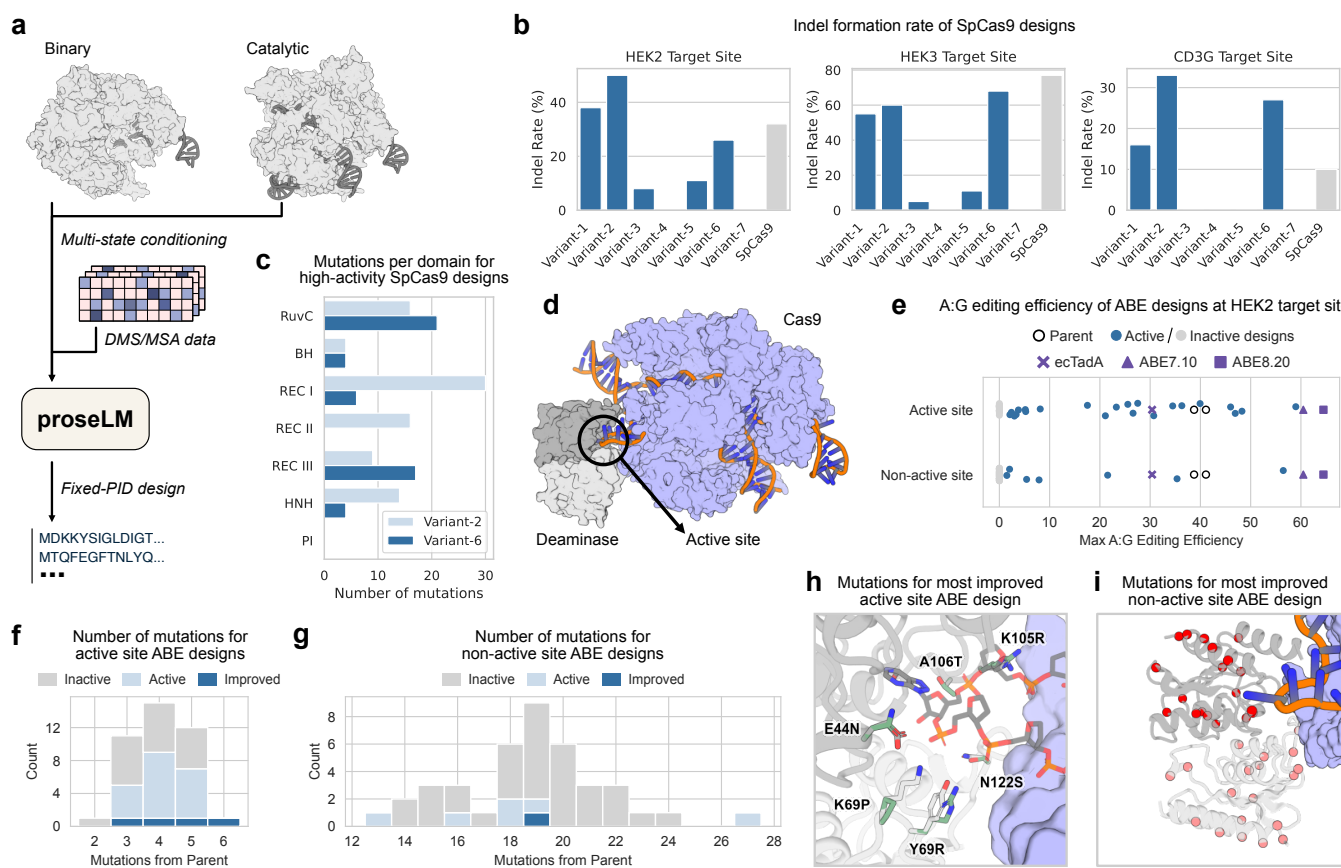


**Figure 3. Optimization of genome editors with proseLM.** (a) Methodology for design of SpCas9 nuclease variants. Sequences were generated from ProseLM with conditioning on the binary and catalytic states from PDB IDs 4ZT0 and 7Z4J, respectively, and positional residue frequencies from natural sequences (MSA) and experimental data (DMS). The PAM-interacting domain residues were fixed to maintain compatibility with SpCas9 target sites. (b) Editing efficiency of seven designed Cas9 variants across three target sites, with comparisons to parental SpCas9. Five of seven designs showed some activity across at least two guides. (c) Distribution of mutations across SpCas9 domains for two high-activity nuclease designs, with 102 and 59 total mutations. (e) Structure of adenine base editor (PDB ID 6VPC), with deaminase active site highlighted. (e) Maximum A-to-G editing efficiency for deaminases with design focused on active site or non-active site residues. The parental deaminase activity is indicated by open circles, while active and inactive designs are indicated by blue and gray circles, respectively. The editing efficiencies of three deaminases designed through directed evolution (26, 27) are indicated by purple markers. (f) Number of mutations from parental deaminase for experimentally tested active site designs. Number of designs with observable and improved activity are indicated by light and dark blue bars, respectively. (g) Number of mutations from parental deaminase for experimentally tested non-active site designs. Number of designs with observable and improved activity are indicated by light and dark blue bars, respectively. (h) Structural model of active site six mutations that resulted in highest A:G editing efficiency. Parental residues and mutations are shown in gray and green, respectively. (i) Positions of 19 mutations at non-active site positions that resulted in highest A:G editing efficiency.

199 previously characterized target sites. Across all three sites, we observed a wide range of editing efficiencies,  
200 with a subset of variants showing activity on-par or higher than SpCas9 (Figure 3b). The most active  
201 variant, Variant-2, showed a significant increase in editing compared to wild-type SpCas9 at two of three  
202 target sites. Notably, this variant contained considerable mutational load in the REC-1 and HNH domains  
203 (Figure 3c), which may facilitate higher on-target editing through reduced specificity and increased nuclease  
204 activity.

205 We next considered the design of base editors, which are fusions of a deaminase domain to a Cas9 nickase  
206 scaffold (26) (Figure 3d). Adenine base editors enable the targeted conversion of A:T base pairs to G:C base  
207 pairs in the genome, and have been used to correct pathogenic mutations in human cells (27). As a testbed  
208 for optimization with proseLM, we selected a deaminase domain previously designed using protein language  
209 models (16) with editing activity on par with early base editors derived from the natural *E. coli* TadA

210 protein (26). We created a structural model of the base editor functional state by aligning an AlphaFold2  
211 (9) prediction of the dimeric deaminase complex to the previously solved structure of ABE8e (28). Using  
212 proSeLM, we then focused design on active site residues (within 5 Å of the bound adenine) or non-active site  
213 residues (outside 5 Å and not in the deaminase dimer interface). We tested 40 designs from each strategy  
214 for A-to-G editing efficiency in HEK293T cells and found that both strategies yielded base editors with  
215 nearly 50% higher editing efficiency than the parental deaminase (Figure 3e). Among the active site designs,  
216 improvements in editing efficiency were achieved with as few as three mutations, while the best design  
217 featured six mutations (Figure 3f). For non-active site designs, which ranged from 13 to 27 mutations, fewer  
218 designs retained editing efficiency and only one showed improvement over the parental sequence (Figure 3g).  
219 In Figure 3h, the set of six active-site mutations yielding a 50% relative improvement in editing efficiency  
220 are depicted on the predicted structure of the parental deaminase. While it is difficult to ascertain the  
221 precise contribution of each mutation, the design contains several non-conservative mutations, representing  
222 a significant reworking of functionally important residues. Meanwhile, the non-active site design with the  
223 highest editing efficiency contained 19 mutations distributed across the surface and core of the deaminase  
224 (Figure 3i), which may facilitate increased editing through stabilization of the domain.

225 **Therapeutic antibody design.** Antibodies are a class of immune proteins that have been developed for a  
226 wide range of research and clinical applications. The design of specific and biophysically well-behaved  
227 antibodies has been a long-standing challenge, due in large part to the complexity and sensitivity of protein-  
228 protein interactions typical of antibody-antigen complexes. Recently, protein language models (including  
229 antibody-specific models) have been used for targeted optimization of particular antibody attributes, such  
230 as stability (29) or immunogenicity (30). However, prior approaches have primarily focused on sequence-  
231 based optimization, ignoring the structural context of antibody binding, and focusing on mutations to the  
232 framework region. We reasoned that by explicitly modeling the antibody-antigen interface, proSeLM would  
233 be well-suited for optimization of the binding affinity of therapeutic antibodies.

234 Although proSeLM models effectively recovered native residues at protein-protein interfaces, neither the  
235 causal encoder nor the ProGen2 models were exposed to significant numbers of antibody sequences during  
236 training. To address this limitation, we trained proSeLM-Ab (based on adaptation of the ProGen2-OAS  
237 model) on a set of antibody structures from the Structural Antibody Database (SAbDab) (31). We  
238 compared the perplexity of ProGen2 and proSeLM models on a held-out set of antibodies and found that  
239 proSeLM-Ab achieved lower perplexity than proSeLM models trained on the PDB, including those with  
240 significantly more parameters (Figure 4a). These improvements came despite the underlying ProGen2-OAS  
241 model assigning relatively high perplexity to the held-out antibodies, likely due to an under-representation  
242 of light chains in its training corpus (13, 32). When provided antigen context, all proSeLM models assigned  
243 lower perplexity to the antibody sequences (Figure 4b) and typically achieved higher rates of native sequence  
244 recovery (Figure 4c). For heavy and light chain framework regions, we observed a scaling trend in sequence  
245 recovery, with larger models achieving higher recovery rates (Figure 4d). For CDR regions, we observed a  
246 similar trend, although the recovery rates were generally lower than for the framework regions. ProSeLM-Ab  
247 frequently achieved the highest rates of recovery for CDR loops, but showed the largest improvements in  
248 the framework regions, demonstrating the utility of adapting antibody-specific language models trained on  
249 diverse antibody sequences.

250 To test the design capabilities of proSeLM models, we first considered affinity optimization of the  
251 therapeutic antibody nivolumab, which targets the PD-1 antigen. We focused mutations in either the  
252 complementarity-determining regions (CDRs) or the framework regions. For CDR-directed designs, we  
253 considered all single and double mutations (excluding mutations to or from cysteine or proline) at positions  
254 within 8 Å of the antigen (Figure S9). For framework variants, we redesigned the entire heavy and light  
255 chain variable fragments, conditioned on the residues within 8 Å of the antigen (Figure S10). Designs from  
256 both strategies were scored using an ensemble of proSeLM models and the best 55 CDR-directed and 40  
257 framework-directed variants were selected for experimental characterization. We tested for binding to PD-1  
258 via surface plasmon resonance (SPR) and obtained  $K_D$  values for 25.4% of CDR-directed designs and 92.5%

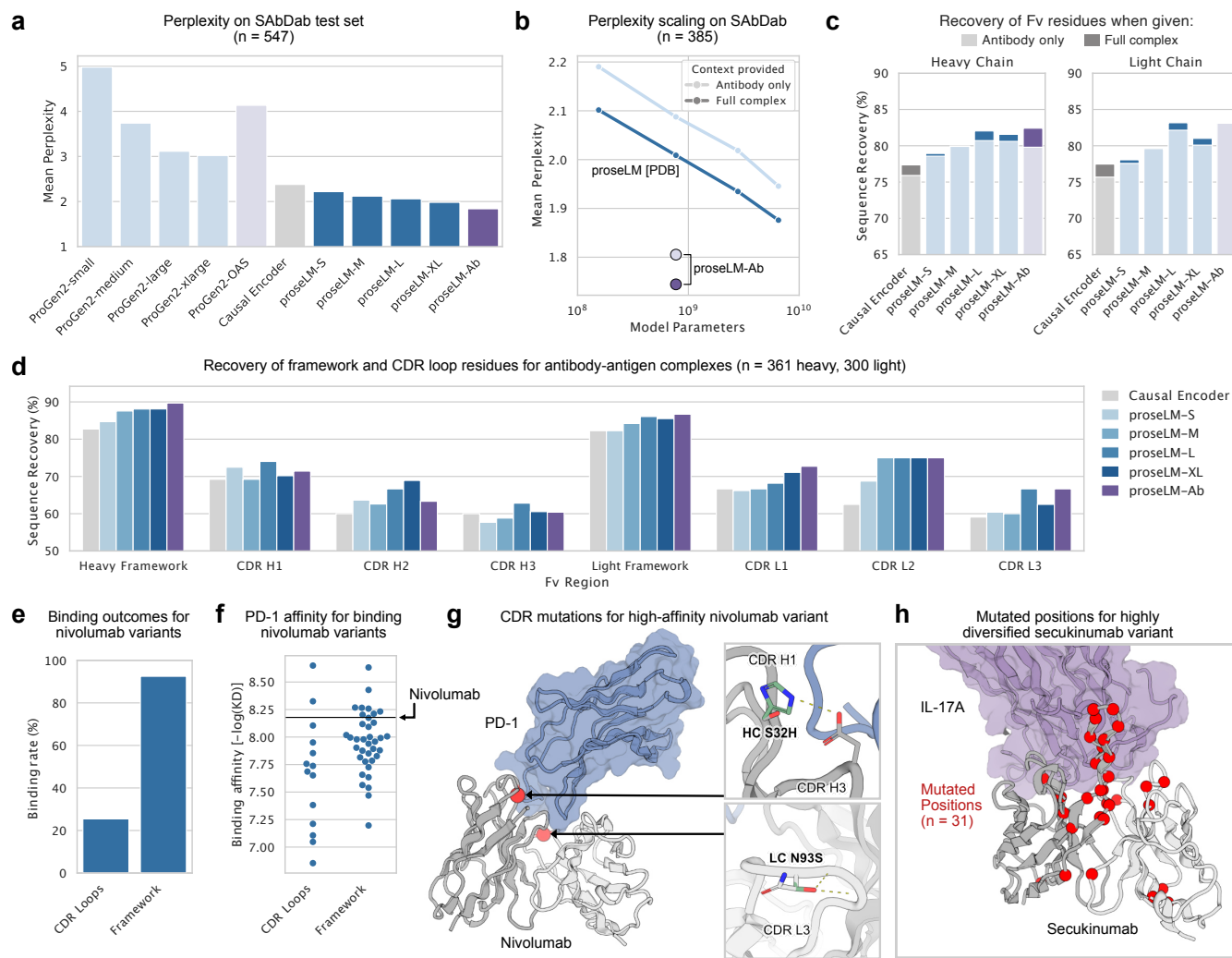


**Figure 4. Design of therapeutic antibodies with proseLM.** All perplexity and sequence recovery values are reported as the mean and median, respectively, of cluster-averaged values. (a) Perplexity of proseLM models on the antibody dataset collected from SAbDab. For all models, perplexity decreases when antigen context is provided. (b) Perplexity with respect to total model parameters for proseLM models with and without antigen context provided. Blue lines and purple points represent performance of PDB-trained (proseLM [PDB]) and SAbDab-trained (proseLM-Ab) models, respectively. (c) Native sequence recovery for fully designed heavy and light chain variable fragment sequences, with and without antigen context. (d) Sequence recovery for designed heavy and light chain variable fragments by structural region. (e) Percentage of experimentally tested nivolumab variants that retained PD-1 binding for each design strategy. (f) Binding affinity (-log(KD), higher better) for nivolumab variants that retained PD-1 binding. Horizontal line indicates the binding affinity of the parental nivolumab antibody. (g) Structural model of mutations for highest affinity nivolumab variant from CDR-directed optimization strategy. The locations of the two mutations in the Fv are shown as red spheres, with potential novel interactions highlighted. (h) Position of mutations for highly diversified secukinumab variant, with 31 positions mutated across the heavy and light chains.

of framework-directed designs (Figure 4e). Among these, we observed a wide range of binding affinities, with the most improved variants from each strategy achieving a nearly three-fold increase in binding affinity relative to nivolumab (Figure 4f). The most improved CDR-directed variant contained two mutations near the antigen interface, which likely facilitated tighter binding through improved rigidification of the paratope (Figure 4g), despite one mutation (HC S32H) ablating binding and the other (LC N93S) only moderately improving affinity in isolation. The most improved framework-directed variant contained seven mutations that may have indirectly improved binding through stabilization of the framework (33).

Given the success of targeted optimization of nivolumab binding affinity, we next considered a more aggressive redesign strategy for a more structurally challenging therapeutic antibody. For this task, we selected secukinumab, which binds the IL-17A cytokine through contacts mediated by an extended 18-residue

269 CDR H3 loop. Rather than target specific residues for redesign, we used proseLM to directly redesign the  
270 entire heavy and light chain variable fragments of secukinumab (Figure S11). Due to the relative ease of  
271 recovering framework residues, the majority of variation was focused within the CDR loops (particularly  
272 CDR H3). We tested 96 designs for binding to IL-17A via SPR and found two variants that retained binding  
273 (Figure 4h). These variants contained 18 and 31 mutations and bound with 135 nM and 102 nM affinity,  
274 respectively. While further optimization of these variants would be necessary to achieve therapeutically  
275 relevant binding affinities, these results demonstrate the potential of proseLM for the diversification of  
276 structurally challenging therapeutic antibodies.

## 277 Discussion

278 Recent generative models for structure-based protein design have shown promise for a variety of design tasks  
279 (3), but are ultimately limited by the quantity and diversity of structures used for training (4). Protein  
280 language models, which learn directly from sequences, have been shown to implicitly capture the structural  
281 and functional constraints of proteins (11, 13) and are capable of generating functional proteins (14–16).  
282 However, steering protein language models towards a particular fold or function typically requires curation  
283 of natural examples for fine-tuning, which may be limited or non-existent for some design tasks. In this  
284 work, we presented proseLM, a method for providing explicit structural and functional context to protein  
285 language models for structure-conditioned design and showed that the sequence generation capabilities of  
286 proseLM benefit from the scaling trends of the underlying language models. Prior work has attempted  
287 to circumvent the paucity of experimental structure data by leveraging highly accurate protein structure  
288 prediction models, such as AlphaFold2 (9), to generate synthetic training data for protein design models  
289 (4). While this approach yielded higher native sequence recovery, the usage of synthetic data may introduce  
290 biases that limit the practical utility of the resulting models (34). By contrast, proseLM leverages the wealth  
291 of protein sequence data directly, enabling more efficient post hoc incorporation of structural awareness.

292 In validating proseLM, we selected design tasks where functional context was not only critical, but also  
293 where recapitulating the native sequence was not sufficient for success. For optimization of SpCas9, this  
294 entailed navigating the local fitness landscape of a protein that is already highly performant. Here, we found  
295 that proseLM designs largely retained activity, in some cases improving on-target editing efficiency. Further  
296 testing is required to determine the off-target editing profile of these variants, but these results suggest that  
297 proseLM can be used to identify functionally relevant mutations in complex protein-nucleic acid systems.  
298 For base editor optimization, our starting point was a generated deaminase with activity that already does  
299 not exist in nature (deamination of single-stranded DNA). Here, we found that proseLM could be used to  
300 directly redesign the active site of the deaminase, yielding variants with significantly increased activity.  
301 These results suggest that proseLM can be used in design settings where function deviates from nature,  
302 provided a reasonable structural hypothesis. Finally, for antibody design tasks, we began with therapeutic  
303 antibodies that are already highly optimized for their intended functions. Against this strong baseline, we  
304 found that proseLM could be used to improve binding affinity through CDR-directed or framework-directed  
305 optimization, as well as to diversify the binding region of a structurally complex antibody. Overall, these  
306 results demonstrate the utility of proseLM for a variety of functional protein design tasks.

307 Language models have excelled at functional protein design by implicitly modeling structural and  
308 functional constraints through fine-tuning on curated examples. As we move towards making these  
309 constraints explicit, we anticipate trade offs will emerge in cases where it is difficult to precisely and  
310 sufficiently specify the desired functional behavior. In this work, we saw evidence of this tradeoff for fitness  
311 prediction, where proseLM models trained with only the protein backbone outperformed those that were  
312 explicitly conditioned on functional context during training. This discrepancy was most pronounced for  
313 binding datasets, for which fitness is directly tied to an interaction with a specific partner. In light of this,  
314 we expect that backbone-only proseLM models will be more useful for design settings where the desired  
315 function is challenging to specify structurally, but is consistent with natural evolutionary constraints of the  
316 protein family. Meanwhile, for tasks where the desired function is novel or highly specific, we anticipate that

317 explicit conditioning on functional context will be necessary. In the future, models that can incorporate  
318 categorical or partial structural conditioning may facilitate the design of proteins with more complex  
319 functional requirements.

## 320 **Data availability**

321 Protein structure datasets used for training the models described in this work are available from public  
322 sources as detailed in the Methods. Designed protein sequences and experimental outcomes are available in  
323 the Supplementary Information.

## 324 **Code availability**

325 Original code and trained models described in this work will be made available at <https://github.com/Profluent-AI/proseLM-public>.

## 327 **Author contributions**

328 J.A.R. conceived of the project. A.M. supervised the project. J.A.R. developed the methodology and  
329 conducted the investigation. A.B. contributed to the methodology. A.B., J.B., and S.N. contributed to the  
330 design and selection of Cas9 proteins. J.A.R. performed design and selection of base editors and antibodies.  
331 J.G. designed wet lab experiments. J.R., E.H., R.H., and J.G. performed wet lab characterization of genome  
332 editing proteins. S.N. processed experimental genome editing data. J.A.R. wrote the first draft of the  
333 manuscript. All authors wrote and/or reviewed the final draft of the manuscript.

## 334 **Competing interests**

335 The authors are current or former employees, contractors, or executives of Profluent Bio Inc and may hold  
336 shares in Profluent Bio Inc.

## 337 **Safety and ethics**

338 Computational protein design carries the dual potential to accelerate development of novel therapeutics and  
339 other society-improving molecules, while providing parallel capabilities for nefarious uses, such as engineering  
340 of bioweapons. When bolstered by current and future iterations of generative AI, these capabilities are  
341 heightened and expected to grow further. The global protein design community has begun to establish  
342 appropriate regulations and guidelines towards the continued beneficial development and application of  
343 these technologies. In support of these efforts, J.A.R. and A.M. have joined as signatories on a set of  
344 community values, guiding principles, and commitments for the responsible development of AI for protein  
345 design (<https://responsiblebiodesign.ai/>). Gene synthesis represents a critical step in the actualization  
346 of designed protein sequences. The International Gene Synthesis Consortium (IGSC) unites major gene  
347 synthesis providers under a commitment to screen all incoming orders against known pathogens and  
348 potentially dangerous sequences. As a concrete step towards safe application of protein design technology,  
349 all gene synthesis work in support of the present study was performed with IGSC members. For all  
350 protein design projects, we urge researchers to maintain ethical oversight throughout project initiation,  
351 experimental characterization, and subsequent deployment phases to ensure safety and avoid unintended  
352 harmful outcomes.

## 353 **Methods**

354 **Protein structure datasets.** Three datasets were assembled for training proseLM models: single-chain  
355 proteins, protein complexes with non-protein context, and antibody complexes. For training on diverse  
356 single-chain proteins, we used the CATH 4.2 dataset constructed by Ingraham et al. (2), which has  
357 been widely adopted as a benchmark for single-chain protein design methods (3, 22, 35). For training on

358 protein complexes with non-protein context, we adapted the dataset used to train multi-chain variants of  
359 ProteinMPNN (3). This dataset was originally constructed by clustering the entire PDB – as of August  
360 2, 2021 – at 40% sequence identity and identifying clusters for testing that did not include proteins that  
361 co-occurred in biological assemblies with proteins used for training. We extended this dataset by extracting  
362 non-protein context within 5 Å of the protein chains. For training on antibody complexes, we collected all  
363 antibody structures from SAbDab (31) – as of July 1, 2023 – and performed clustering at 80% identity on  
364 the concatenated heavy and light chain variable fragment sequences with MMseqs2 (36). These clusters  
365 were used to divide the dataset into training, validation, and test splits, such that roughly 80%, 10%, and  
366 10% of clusters were allocated to each split, respectively.

### 367 **Model architecture.**

368 **Structure featurization.** We formulate protein structures as nearest-neighbor graphs, with residues as nodes  
369 and inter-residue relationships as edges. The graph adjacency matrix is defined by the proximity of residues  
370 in sequential and three-dimensional space. For each residue, we first take the six closest residues along  
371 the sequence then the next thirty closest residues according to  $C_\alpha$  distance, for a total of 36 neighbors. The  
372 nodes are featurized only with a binary indicator of whether the residue has a backbone structure (i.e., N,  
373  $C_\alpha$ , and C atoms). The edges are featurized by the inter-residue distances between pairs of backbone atoms  
374 (N,  $C_\alpha$ , C, O, and virtual  $C_\beta$ ) and an embedding indicating the relative position of neighboring residues  
375 along the sequence, up to a maximum of 32 positions in either direction. For inter-chain residue pairs, we  
376 set the relative positional embedding to a constant value indicating no sequential relationship, but all other  
377 features remain the same.

378 For atomic-level representation of non-protein context, we adopt a similar graph representation, with  
379 individual atoms as nodes and inter-atomic relationships as edges. The adjacency matrix for the atomic  
380 graph is constructed by selecting the ten nearest atoms in three-dimensional space. Each atom is represented  
381 as a node with an associated reference frame formed by the atom-of-interest and its two nearest neighbors.  
382 The nodes are initialized with the types of each atom, along with the distances between the primary atom  
383 and its neighbors. The edges of the atomic graph are featurized by the inter-atomic distances between these  
384 triplets of atoms. Finally, to incorporate information from the atomic graph into the protein graph, we  
385 construct a cross-graph adjacency matrix between each protein residue and the nearest thirty atoms (up to  
386 12 Å away) in the atomic graph. The edges for the protein-atomic graph are featurized by the pairwise  
387 distances between the backbone atoms of the protein residues and the atom triplets of the atomic graph.

388 **Causal encoder architecture.** The causal encoder takes as input the protein and atomic context graphs  
389 featurized as described above. All discrete node and edge features (binary structural indicator, relative  
390 positional embedding, etc.) are one-hot encoded. All distance-based edge features are encoded by sets of  
391 sixteen Gaussian radial basis functions (RBFs) equally spaced between 0 and 20 Å. The respective features  
392 for nodes and edges are concatenated then processed by two-layer MLPs to bring them to appropriate  
393 dimensionality. As in prior work (2, 3), the causal encoder is composed of a series of sequence-agnostic  
394 encoder layers followed by a series of causally masked decoder layers that are ultimately used to predict  
395 the amino acid sequence (Algorithm 1). Complete hyperparameters for the causal encoder are provided in  
396 Table 1.

397 The encoder and decoder layers are parameterized by graph neural networks (GNNs), specifically taking  
398 the form of message-passing neural network (MPNN) layers (2, 3) and invariant point message-passing  
399 (IPMP) layers (20). Our instantiation of MPNN and IPMP layers differ only in the features used to form  
400 messages for updating node and edge embeddings. For MPNN layers, messages are formed by concatenating  
401 node and edge embeddings for neighbors in the graph topology (Algorithm 2). For IPMP layers, we add to  
402 these embeddings the set of five invariant components proposed by Randolph et al. (20) (Algorithm 3). To  
403 obtain these components, we predict a set of invariant points in the local frame of each node, then compute  
404 the following for each pair of neighboring nodes in the graph (Algorithm 4):

---

**Algorithm 1** Causal encoder
 

---

**Require:**  $\mathbf{n}_i^{\text{prot}}, \mathbf{e}_{ij}^{\text{prot}}$  ▷ Protein node and edge embeddings  
**Require:**  $\mathbf{n}_i^{\text{atom}}, \mathbf{e}_{ij}^{\text{atom}}$  ▷ Atomic node and edge embeddings  
**Require:**  $\mathbf{e}_{ij}^{\text{prot-atom}}$  ▷ Protein-atomic edge embeddings  
**Require:**  $\mathbf{T}_i^{\text{prot}}, \mathbf{T}_i^{\text{atom}}$  ▷ Rigid transforms for protein and atomic nodes  
**Require:**  $\mathcal{N}^{\text{prot}}, \mathcal{N}^{\text{atom}}, \mathcal{N}^{\text{prot-atom}}$  ▷ Topology of protein, atomic, and protein-atomic graphs  
**Require:**  $\mathbf{s}_i^{\text{prot}}$  ▷ Amino acid sequence

**for**  $l \in N_{\text{enc\_layers}}$  **do**

# *Update protein nodes and edges*

$\mathbf{n}_i^{\text{prot}}, \mathbf{e}_{ij}^{\text{prot}} \leftarrow \text{ProteinMPNLayer}^{(l)}(\mathbf{n}_i^{\text{prot}}, \mathbf{e}_{ij}^{\text{prot}}, \mathcal{N}^{\text{prot}})$

$\mathbf{n}_i^{\text{prot}}, \mathbf{e}_{ij}^{\text{prot}} \leftarrow \text{ProteinIPMPLayer}^{(l)}(\mathbf{n}_i^{\text{prot}}, \mathbf{e}_{ij}^{\text{prot}}, \mathbf{T}_i^{\text{prot}}, \mathcal{N}^{\text{prot}})$

if Exists( $\mathbf{n}_i^{\text{atom}}, \mathbf{e}_{ij}^{\text{atom}}, \mathbf{e}_{ij}^{\text{prot-atom}}$ ) **then**

# *Update atomic nodes and edges*

$\mathbf{n}_i^{\text{atom}}, \mathbf{e}_{ij}^{\text{atom}} \leftarrow \text{AtomIPMPLayer}^{(l)}(\mathbf{n}_i^{\text{atom}}, \mathbf{e}_{ij}^{\text{atom}}, \mathcal{N}^{\text{atom}})$

# *Update protein nodes and protein-atomic edges*

$\mathbf{n}_i^{\text{prot}}, \mathbf{e}_{ij}^{\text{prot-atom}} \leftarrow \text{CrossIPMPLayer}^{(l)}(\mathbf{n}_i^{\text{prot}}, \mathbf{n}_i^{\text{atom}}, \mathbf{e}_{ij}^{\text{prot-atom}}, \mathbf{T}_i^{\text{atom}}, \mathbf{T}_i^{\text{atom}}, \mathcal{N}^{\text{prot-atom}})$

$\mathbf{s}_{ij}^{\text{prot}} \leftarrow \text{CausalMask}(\text{Linear}(\mathbf{s}_i^{\text{prot}}, \mathcal{N}^{\text{prot}}))$  ▷ Embed sequence on edges and causally mask

$\mathbf{e}_{ij}^{\text{prot}} \leftarrow \mathbf{e}_{ij}^{\text{prot}} + \text{Linear}(\text{Concat}(\mathbf{e}_{ij}^{\text{prot}}, \mathbf{s}_{ij}^{\text{prot}}))$  ▷ Update protein edges with sequence embedding

**for**  $l \in N_{\text{dec\_layers}}$  **do**

# *Update protein nodes and edges for decoding*

$\mathbf{n}_i^{\text{prot}}, \mathbf{e}_{ij}^{\text{prot}} \leftarrow \text{ProteinMPNLayer}^{(l)}(\mathbf{n}_i^{\text{prot}}, \mathbf{e}_{ij}^{\text{prot}}, \mathcal{N}^{\text{prot}})$

$\mathbf{n}_i^{\text{prot}}, \mathbf{e}_{ij}^{\text{prot}} \leftarrow \text{ProteinIPMPLayer}^{(l)}(\mathbf{n}_i^{\text{prot}}, \mathbf{e}_{ij}^{\text{prot}}, \mathbf{T}_i^{\text{prot}}, \mathcal{N}^{\text{prot}})$

$\tilde{\mathbf{s}}_i \leftarrow \text{Linear}(\mathbf{n}_i^{\text{prot}})$  ▷ Predict amino acid sequence

**return**  $\tilde{\mathbf{s}}_i, \mathbf{n}_i^{\text{prot}}$  ▷ Return predicted sequence and causally informed protein nodes

---

**Table 1. Causal encoder hyperparameters.**

Category	Hyperparameter	Value
Graph topology	Protein sequential neighbors	6
	Protein spatial neighbors	30
	Atomic spatial neighbors	30
	Protein-atomic spatial neighbors	30
Architecture	Number of encoder layers, $N_{enc\_layers}$	3
	Number of decoder layers, $N_{dec\_layers}$	3
All GNN layers	Node message MLP layers	3
	Edge message MLP layers	3
	Node update MLP layers	2
	Edge update MLP layers	2
	Node embedding dimension	128
	Edge embedding dimension	128
Protein GNN layers	Node message MLP hidden dimension	128
	Edge message MLP hidden dimension	128
	Node update MLP hidden dimension	512
	Edge update MLP hidden dimension	128
	IPMP invariant points	8
	Node embedding dimension	16
	Edge embedding dimension	16
	Node message MLP hidden dimension	16
	Edge message MLP hidden dimension	16
	Node update MLP hidden dimension	64
Atomic GNN layers	Edge update MLP hidden dimension	16
	IPMP invariant points	4
	Node embedding dimension	128
	Edge embedding dimension	16
	Node message MLP hidden dimension	16
	Edge message MLP hidden dimension	16
Protein-atomic GNN layers	Node update MLP hidden dimension	64
	Edge update MLP hidden dimension	16
	IPMP invariant points	4
	Node embedding dimension	128
	Edge embedding dimension	16
	Node message MLP hidden dimension	16

- 405 1. Node  $i$ 's invariant points in node  $i$ 's local frame  
 406 2. Distances from node  $i$ 's invariants points to the origin of node  $i$ 's local frame  
 407 3. Node  $j$ 's invariant points in node  $i$ 's local frame  
 408 4. Distances from node  $j$ 's invariant points to the origin of node  $i$ 's local frame  
 409 5. Distances between node  $i$ 's invariant points and node  $j$ 's invariant points in the global frame

410 After assembling the message features  $\mathbf{p}_{ij}$  for MPNN or IPMP layers, we pass those features through a  
 411 set of common operations to update node then edge embeddings. For the node embeddings, we compute  
 412 a set of messages  $\mathbf{m}_{ij}$  for each neighboring node  $j \in \mathcal{N}$  using a three-layer MLP and aggregate them by  
 413 taking the mean across all neighbors. These messages are then added to the original node embeddings and  
 414 passed through a layer normalization. The updated node embeddings are further processed by a two-layer  
 415 MLP, with the outputs added back to the previously updated node embeddings with layer normalization.  
 416 For the edges, we follow a similar procedure but omit the aggregation step and instead directly update the  
 417 embeddings using the messages.

418 To enable the decoder layers to predict the amino acid sequence residue-by-residue at inference time, we  
 419 provide the ground truth (or presently decoded) sequence through causally masked edge embeddings (2).  
 420 Specifically, for neighboring nodes  $i > j$ , the protein sequence  $\mathbf{s}_i^{prot}$  is embedded and added to the protein  
 421 edges. For node and edge updates, we form messages in a causally consistent manner for neighboring nodes  
 422  $i$  and  $j$  by selectively using encoder node embeddings for node  $j$  when  $i < j$  and decoder node embeddings  
 423 when  $i > j$ . The final node embeddings are used to predict the amino acid sequence through a linear layer.

---

**Algorithm 2** MPNN layer
 

---

**Require:**  $\mathbf{n}_i, \mathbf{e}_{ij}$  ▷ Node and edge embeddings  
**Require:**  $\mathcal{N}$  ▷ Topology of graph specifying neighbors of each node

*# Node update*

$$\begin{aligned} \mathbf{p}_{ij} &\leftarrow \text{Concat}_{j \in \mathcal{N}(i)}(\mathbf{n}_i, \mathbf{n}_j, \mathbf{e}_{ij}) \\ \mathbf{m}_{ij} &\leftarrow \text{NodeMessageMLP}(\mathbf{p}_{ij}) \\ \mathbf{m}_i &\leftarrow \text{Mean}_j(\mathbf{m}_{ij}) \\ \mathbf{n}_i &\leftarrow \text{LayerNorm}(\mathbf{n}_i + \mathbf{m}_i) \\ \mathbf{n}_i &\leftarrow \text{LayerNorm}(\mathbf{n}_i + \text{NodeUpdateMLP}(\mathbf{n}_i)) \end{aligned}$$

*# Edge update*

$$\begin{aligned} \mathbf{p}_{ij} &\leftarrow \text{Concat}_{j \in \mathcal{N}(i)}(\mathbf{n}_i, \mathbf{n}_j, \mathbf{e}_{ij}) \\ \mathbf{m}_{ij} &\leftarrow \text{EdgeMessageMLP}(\mathbf{p}_{ij}) \\ \mathbf{e}_{ij} &\leftarrow \text{LayerNorm}(\mathbf{e}_{ij} + \mathbf{m}_{ij}) \\ \mathbf{e}_{ij} &\leftarrow \text{LayerNorm}(\mathbf{e}_{ij} + \text{EdgeUpdateMLP}(\mathbf{e}_{ij})) \end{aligned}$$

**return**  $\mathbf{n}_i, \mathbf{e}_{ij}$

---

**Algorithm 3** IPMP layer
 

---

**Require:**  $\mathbf{n}_i, \mathbf{e}_{ij}$  ▷ Node and edge embeddings  
**Require:**  $\mathbf{T}_i$  ▷ Rigid transforms  
**Require:**  $\mathcal{N}$  ▷ Topology of graph specifying neighbors of each node

*# Node update*

$$\begin{aligned} \mathbf{p}_{ij} &\leftarrow \text{IPMPMessageFn}(\mathbf{n}_i, \mathbf{e}_{ij}, \mathbf{T}_i, \mathcal{N}) \\ \mathbf{m}_{ij} &\leftarrow \text{NodeMessageMLP}(\mathbf{p}_{ij}) \\ \mathbf{m}_i &\leftarrow \text{Mean}_j(\mathbf{m}_{ij}) \\ \mathbf{n}_i &\leftarrow \text{LayerNorm}(\mathbf{n}_i + \mathbf{m}_i) \\ \mathbf{n}_i &\leftarrow \text{LayerNorm}(\mathbf{n}_i + \text{NodeUpdateMLP}(\mathbf{n}_i)) \end{aligned}$$

*# Edge update*

$$\begin{aligned} \mathbf{p}_{ij} &\leftarrow \text{IPMPMessageFn}(\mathbf{n}_i, \mathbf{e}_{ij}, \mathbf{T}_i, \mathcal{N}) \\ \mathbf{m}_{ij} &\leftarrow \text{EdgeMessageMLP}(\mathbf{p}_{ij}) \\ \mathbf{e}_{ij} &\leftarrow \text{LayerNorm}(\mathbf{e}_{ij} + \mathbf{m}_{ij}) \\ \mathbf{e}_{ij} &\leftarrow \text{LayerNorm}(\mathbf{e}_{ij} + \text{EdgeUpdateMLP}(\mathbf{e}_{ij})) \end{aligned}$$

**return**  $\mathbf{n}_i, \mathbf{e}_{ij}$

---

---

**Algorithm 4** Invariant point message features

---

**Require:**  $\mathbf{n}_i, \mathbf{e}_{ij}$  ▷ Node and edge embeddings  
**Require:**  $\mathbf{T}_i$  ▷ Rigid transforms  
**Require:**  $\mathcal{N}$  ▷ Topology of graph specifying neighbors of each node

```

 $\mathbf{x}_i \leftarrow \text{Linear}(\mathbf{n}_i)$  ▷ Invariant points in  $i$ 's local frame
 $\mathbf{d}_i^{\text{origin}} \leftarrow \|\mathbf{x}_i\|_2$  ▷ Distances from  $i$ 's points to  $i$ 's origin
 $\mathbf{x}_{ij} \leftarrow \mathbf{T}_i^{-1} \circ \mathbf{T}_j \circ \mathbf{x}_j$  ▷ Node  $j$ 's points in  $i$ 's local frame
 $\mathbf{d}_{ij}^{\text{origin}} \leftarrow \|\mathbf{T}_i^{-1} \circ \mathbf{T}_j \circ \mathbf{x}_j\|_2$  ▷ Distances from  $j$ 's points in  $i$ 's local frame to  $i$ 's origin
 $\mathbf{d}_{ij}^{\text{points}} \leftarrow \|\mathbf{T}_i \circ \mathbf{x}_i - \mathbf{T}_j \circ \mathbf{x}_j\|_2$  ▷ Distances between  $i$ 's points and  $j$ 's points in global frame
 $\mathbf{p}_{ij} \leftarrow \text{Concat}_{j \in \mathcal{N}(i)}(\mathbf{n}_i, \mathbf{n}_j, \mathbf{e}_{ij}, \mathbf{x}_i, \mathbf{d}_i^{\text{origin}}, \mathbf{x}_{ij}, \mathbf{d}_{ij}^{\text{origin}}, \mathbf{d}_{ij}^{\text{points}})$ 
return  $\mathbf{p}_{ij}$ 

```

---

424 Causal encoder models were trained for 80 epochs on the CATH 4.2 and PDB datasets with an effective  
425 batch size of 32 using the Adam optimizer (37). The learning rate was increased linearly over 4,000 warmup  
426 steps to a maximum value of 1e-4, then decayed according to an inverse-square-root schedule. An additional  
427 set of models were trained in the same manner but with 0.1 Å Gaussian noise added to the protein backbone  
428 coordinates. The final models were chosen according to validation set loss.

429 **ProseLM architecture.** For proseLM models, we combine a pre-trained causal encoder with a pre-trained  
430 ProGen2 protein language model (13) using a set of parameter-efficient conditional adapters (Algorithm 5).  
431 The causal encoder is used to encode the protein and atomic structures, as well as the causally masked  
432 amino acid sequence, into a set of node embeddings  $\mathbf{n}_i^{\text{prot}}$ . These embeddings are then used to condition the  
433 outputs of the simultaneous attention and feedforward layers of the language model through a set of MLP  
434 adapters (Algorithm 6). The node embeddings are shifted by one position, such that the language model  
435 is conditioned on the structural information of the next residue to be predicted, rather than the current  
436 residue encoded in the sequence. The adapter layers first down-project the language model embeddings to  
437 a reduced dimensionality, then condition on the node embeddings through a two-layer MLP, and finally  
438 up-project the conditioned embeddings back to the original dimensionality. Importantly, the linear layer  
439 responsible for up-projecting the embeddings is initialized with weights near zero such that the entire  
440 adapter layer approximates an identity operation when training begins. The conditioned embeddings are  
441 ultimately added back to the original language model embeddings and passed through the pre-trained layer  
442 normalization of the language model. Hyperparameters for conditional adapters for each proseLM model  
443 are provided in Table 2.

444 ProseLM models were trained for 5 epochs on the CATH 4.2 dataset and 15 epochs on the PDB dataset  
445 with an effective batch size of 64 using the Adam optimizer (37). The learning rate was set to a fixed value  
446 of 2e-4. An additional set of models were trained in the same manner but with 0.1 Å Gaussian noise added  
447 to the protein backbone coordinates. The final models were chosen according to validation set loss.

**Table 2. ProseLM hyperparameters.**

Model	Language model	LM embed. dim.	Reduction factor	Low-rank embed. dim.
proseLM-S	ProGen2-small	1024	64	16
proseLM-M	ProGen2-medium	1536	96	16
proseLM-L	ProGen2-large	2048	128	16
proseLM-XL	ProGen2-xlarge	4096	256	16
proseLM-Base	ProGen2-base	1536	96	16
proseLM-Ab	ProGen2-OAS	1536	96	16

---

**Algorithm 5** proseLM
 

---

**Require:**  $\mathbf{n}_i^{\text{prot}}$ ,  $\mathbf{e}_{ij}^{\text{prot}}$  ▷ Protein node and edge embeddings  
**Require:**  $\mathbf{n}_i^{\text{atom}}$ ,  $\mathbf{e}_{ij}^{\text{atom}}$  ▷ Atomic node and edge embeddings  
**Require:**  $\mathbf{e}_{ij}^{\text{prot-atom}}$  ▷ Protein-atomic edge embeddings  
**Require:**  $\mathbf{T}_i^{\text{prot}}$ ,  $\mathbf{T}_i^{\text{atom}}$  ▷ Rigid transforms for protein and atomic nodes  
**Require:**  $\mathcal{N}^{\text{prot}}$ ,  $\mathcal{N}^{\text{atom}}$ ,  $\mathcal{N}^{\text{prot-atom}}$  ▷ Topology of protein, atomic, and protein-atomic graphs  
**Require:**  $\mathbf{s}_i^{\text{prot}}$  ▷ Amino acid sequence

*# Encode protein and atomic context*

$$\mathcal{N} \leftarrow \{\mathcal{N}^{\text{prot}}, \mathcal{N}^{\text{atom}}, \mathcal{N}^{\text{prot-atom}}\}$$

$$\mathbf{n}_i^{\text{prot}} \leftarrow \text{CausalEncoder}(\mathbf{n}_i^{\text{prot}}, \mathbf{e}_{ij}^{\text{prot}}, \mathbf{n}_i^{\text{atom}}, \mathbf{e}_{ij}^{\text{atom}}, \mathbf{e}_{ij}^{\text{prot-atom}}, \mathbf{T}_i^{\text{prot}}, \mathbf{T}_i^{\text{atom}}, \mathcal{N}, \mathbf{s}_i^{\text{prot}})$$

*# Language modeling layers*

$$\mathbf{h}_i \leftarrow \text{Linear}(\mathbf{s}_i^{\text{prot}})$$
 ▷ Embed protein sequence

**for**  $l \in N_{\text{LM\_layers}}$  **do**

$$\mathbf{h}_i^{\text{upd}} \leftarrow \text{Attention}^{(l)}(\mathbf{h}_i) + \text{FFNN}^{(l)}(\mathbf{h}_i)$$
 ▷ Simultaneous attention and feedforward layers

$$\mathbf{h}_i^{\text{upd}} \leftarrow \text{MLPAdapter}^{(l)}(\mathbf{h}_i^{\text{upd}}, \mathbf{n}_{i+1}^{\text{prot}})$$
 ▷ Condition on next structure residue

$$\mathbf{h}_i \leftarrow \text{LayerNorm}^{(l)}(\mathbf{h}_i + \mathbf{h}_i^{\text{upd}})$$

$\tilde{\mathbf{s}}_i \leftarrow \text{Linear}(\mathbf{h}_i)$  ▷ Predict amino acid sequence

**return**  $\tilde{\mathbf{s}}_i$

---

**Algorithm 6** MLP adapter
 

---

**Require:**  $\mathbf{h}_i^{\text{upd}}$  ▷ Language model embeddings  
**Require:**  $\mathbf{n}_i^{\text{prot}}$  ▷ Protein node embeddings

$$\mathbf{h}_i^{\text{lr}} \leftarrow \text{Linear}_{\text{down}}(\mathbf{h}_i^{\text{upd}})$$
 ▷ Down-project language model embeddings

$$\mathbf{n}_i^{\text{lr}} \leftarrow \text{Linear}_{\text{down}}(\mathbf{n}_i^{\text{prot}})$$
 ▷ Down-project node embeddings

$$\mathbf{h}_i^{\text{cond}} \leftarrow \text{MLP}(\text{Concat}(\mathbf{h}_i^{\text{lr}}, \mathbf{n}_{i+1}^{\text{lr}}))$$
 ▷ Condition on next structure residue

$$\mathbf{h}_i^{\text{cond}} \leftarrow \text{Linear}_{\text{up}}(\mathbf{h}_i^{\text{cond}})$$
 ▷ Up-project language model embeddings

$$\mathbf{h}_i^{\text{upd}} \leftarrow \mathbf{h}_i^{\text{upd}} + \mathbf{h}_i^{\text{cond}}$$

**return**  $\mathbf{h}_i^{\text{upd}}$

---

448 **Comparison to LM-Design.** The most conceptually similar method to proseLM is LM-Design, which  
449 adapts masked language models for structure-conditioned sequence design (38). While proseLM generates  
450 sequences autoregressively for a given backbone structure, LM-Design adopts a strategy more akin to  
451 sequence refinement using language models given an initial guess. Architecturally, the conditional adapter  
452 of proseLM uses significantly few parameters per layer (80K-300K) than LM-Design (5M per layer). This  
453 discrepancy enables proseLM to maintain parameter-efficiency while incorporating adapters after every  
454 layer of the language model, whereas LM-Design only incorporates adapters after the final layer. To assess  
455 the impact of these architectural differences, we compared proseLM to LM-Design on the CATH 4.2 test  
456 set (Table S1). The most apt comparison to the reported LM-Design performance is proseLM-M, which  
457 contains a similar number of pre-trained language model parameters. We found that proseLM-M achieves  
458 lower perplexity, while LM-Design achieves higher native sequence recovery. This discrepancy likely arises  
459 from the different modeling objectives, with proseLM sampling sequences autoregressively and LM-Design  
460 iteratively updating sequences by sampling from position-wise marginal distributions. Autoregressive  
461 modeling directly captures the co-evolution between pairs of residues, which is critical for protein function,  
462 but may yield designs with lower native sequence recovery.

#### 463 **Design of genome editors.**

464 **Nuclease optimization.** To design optimized SpCas9 nucleases with proseLM, we trained proseLM-Base by  
465 adapting the ProGen2-base model and training on the PDB dataset. This was necessary in order to model  
466 the complete 1,368-residue SpCas9 sequence, which extends beyond the maximum length supported by  
467 other ProGen2 and proseLM models. For design, we utilized a multi-state conditioning strategy, selecting  
468 two structures for conditioning that represented the binary (PDB ID 4ZT0) and catalytic (PDB ID 7Z4J)  
469 states of SpCas9. To account for missing residues in the structures, we used AlphaFold2 to predict the  
470 structures with each state provided as a template. The predicted structures were aligned with sub-Å  
471 RMSD into the experimental complexes, yielding structurally complete representations of the binary and  
472 catalytic states. Using these structures, we designed 1,600 sequences ( $T = 1.0$ ). All sequences were had the  
473 PAM-interacting domain and known catalytic residues fixed to their natural identities.

474 To generate sequences closer to the natural SpCas9 sequence, we introduced positional residue frequencies  
475 derived from evolutionary and experimental data. Evolutionary data was obtained from a multiple-sequence  
476 alignment of phylogenetically related Cas9 proteins, which were used to create a position-specific scoring  
477 matrix (PSSM). Experimental data was obtained from a deep mutational scanning study of SpCas9, which  
478 measured the on- and off-target impacts of single amino acid mutations (39). We combined the PSSM and  
479 normalized DMS data to create a amino acid bias term for each residue in the SpCas9 sequence. This bias  
480 was added to the logits of proseLM-Base and used to generate an additional 4,400 sequences ( $T = 0.1$ ). We  
481 selected the seven designs from this set for experimental characterization according to the criteria used for  
482 OpenCRISPR (16).

483 **Base editor optimization.** For base editor optimization, we selected a deaminase domain previously designed  
484 using protein language models fine-tuned on the TadA family (16). We predicted the structure of the  
485 deaminase dimer using the ABE8e structure (PDB ID 6VPC) as a template, then aligned our predicted  
486 structure into the functional state of the ABE8e complex with sub-Å RMSD. We divided our designs  
487 across two strategies, focusing separately on active site or non-functional scaffolding residues. For active  
488 site designs, we selected all residues within 5 Å of the single-stranded DNA or Cas9 nuclease, excluding  
489 positions at the termini or within 5 Å of the dimeric interface, and kept all other residues fixed. For  
490 non-active site designs, we selected all residues further than 5 Å from the single-stranded DNA or Cas9  
491 nuclease and further than 5 Å from the dimeric interface, and kept all other residues fixed. When generating  
492 designs, we provided the fixed residues to the causal encoder as context by reordering the residue indices,  
493 effectively conditioning proseLM on future positions. We generated 300 active site designs ( $T = 1.0$ ) and  
494 200 non-active site designs ( $T = 0.5$ ) with proseLM-S. The 40 best designs from each strategy according to  
495 perplexity were selected for experimental characterization.

496 **Design of therapeutic antibodies.**

497 **Nivolumab optimization.** To optimize the binding affinity of the therapeutic antibody nivolumab, we used  
498 the crystal structure of nivolumab bound to PD-1 (PDB ID 5WT9). We divided our designs across two  
499 strategies, focusing separately on the complementarity-determining regions (CDRs) and the framework  
500 regions. For CDR-directed designs, we enumerated all possible single- and double-mutations to residues  
501 within 8 Å of the antigen, excluding mutations to or from cysteine or proline. In total, this set included  
502 414,477 variants with mutations across 54 positions. For framework-directed designs, we generated designs  
503 with conditioning on the CDRs by fixing residues within 6 Å of the antigen. We generated 2,000 designs each  
504 from proseLM-Ab and proseLM-Base ( $T = 1.0$ ). Half of the sequences had the heavy chain designed first,  
505 with the light chain successively designed based on the designed heavy, and the other half used the reverse  
506 chain order. We selected 55 CDR-directed and 40 framework-directed designs according to an ensemble of  
507 proseLM models (causal encoder, proseLM-S, proseLM-Base, proseLM-XL, and proseLM-Ab), using the  
508 product of perplexities as a selection criterion. For CDR-directed designs, we selected 15 single mutations  
509 and 40 double mutations. For framework-directed designs, we selected 20 designs with 1-10 mutations and  
510 20 designs with 11-20 mutations. For each strategy, we ensured that no particular mutation appeared more  
511 than ten times in the final set. In total, 95 designs were selected for experimental characterization.

512 **Secukinumab diversification.** For diversification of the therapeutic antibody secukinumab, we used the crystal  
513 structure of secukinumab bound to IL-17A (PDB ID 6WIO). We generated full heavy and light chain  
514 variable fragments with 2,000 designs each from proseLM-Ab and proseLM-Base ( $T = 1.0$ ). Half of the  
515 sequences had the heavy chain designed first, with the light chain successively designed based on the  
516 designed heavy, and the other half used the reverse chain order. From each model's designs, we selected  
517 16 designs with 1-24 mutations, 16 designs with 25-29 mutations, and 16 designs with 30-34 mutations  
518 according to an ensemble of proseLM models (causal encoder, proseLM-S, proseLM-Base, proseLM-XL, and  
519 proseLM-Ab), using the product of perplexities as a selection criterion. In total, 96 designs were selected for  
520 experimental characterization.

521 **Characterization of genome editors.**

522 **DNA oligonucleotides and plasmid assembly.** Oligonucleotides used in this study were synthesized by IDT  
523 with standard desalting. All natural and AI-generated nuclease and deaminase sequences were purchased as  
524 synthetic gene fragments (Twist Bioscience), human codon-optimized using the Twist codon optimization  
525 tool, and cloned into CMV-driven expression plasmids using HiFi DNA Assembly (New England Biolabs).  
526 Single-guide RNA (sgRNA) sequences were cloned into a human U6 (hU6)-driven expression plasmid  
527 that also contains a CMV-driven GFP transfection reporter using HiFi DNA Assembly (New England  
528 Biolabs). All plasmids were sequence-verified by whole plasmid Nanopore sequencing (Primordium) prior  
529 to downstream applications.

530 **HEK293T cell culture and transient transfection.** HEK293T cells (ATCC) were cultured at 37°C and 5% (v/v)  
531 CO<sub>2</sub> in high glucose DMEM with 4 mM L-glutamine, 1 mM sodium pyruvate and phenol red pH indicator  
532 (Gibco), supplemented with 10% FBS and 1X penicillin-streptomycin. 24 hours prior to transfection, cells  
533 were seeded at a density of 1x10<sup>3</sup> cells/well in 96-well tissue culture-treated plates (Nunc<sup>TM</sup> Edge<sup>TM</sup>, Thermo  
534 Fisher Scientific).

535 For each transfection well, 50 ng of sgRNA plasmid and 50 ng of nuclease or base editor-expressing  
536 plasmid were added to 5 µL of Opti-MEM (Gibco). 0.2 µL of TransIT®-2020 transfection reagent (Mirus  
537 Bio) was diluted into 4 µL of Opti-MEM. Plasmid and TransIT®-2020 mixtures were combined, incubated  
538 for 15-30 min at room temperature, and added to HEK293T cells in a dropwise manner. Plates were gently  
539 rocked to mix and incubated for 72 hours.

540 **Targeted-amplicon sequencing and analysis.** Cell lysates were generated by washing the cells with 1X PBS and  
541 adding 25 µL of lysis buffer (100 mM Tris-HCl, pH 7.5; 0.05% SDS; 25 µg/mL Proteinase K) per well. Plates

542 with lysis buffer were incubated at 37°C for 1 hour, and then 25  $\mu$ L of nuclease-free water was added per well.  
543 The lysates were transferred to 96-well PCR plates and boiled at 98°C for 15 min. Locus-specific primers  
544 were used to amplify regions of interest from cell lysates by PCR (Q5® High-Fidelity DNA Polymerase).  
545 After PCR, the resulting amplicons were purified (Mag-Bind® RxnPure Plus, Omega Bio-tek), DNA yields  
546 were quantified (QuantiFluor® kit, Promega), and DNA concentrations were normalized to 2 ng/100 bp  
547 of amplicon length and submitted for Sanger sequencing with the appropriate forward PCR primer. We  
548 quantified the activity of base editors and nucleases using the software tools BEAT (40) and Synthego ICE  
549 v1.2.0 (41), respectively, with default parameters.

## 550 Characterization of antibodies.

551 **Antibody production.** Antibody heavy and light chain variable fragment sequences were synthesized as gene  
552 fragments and cloned into the pTwist CMV vectors. Nivolumab variants were cloned into IgG4 (heavy chain)  
553 and IgK (light chain) vectors. Secukinumab variants were cloned into IgG1 (heavy chain) and IgK (light  
554 chain) vectors. Antibodies were expressed in 1mL HEK293 mammalian cultures and the supernatant was  
555 used for binding affinity measurements. Gene synthesis and expression was performed by Twist Bioscience.

556 **Binding affinity measurements.** Binding studies were performed in HBSTE running buffer (10mM HEPES,  
557 150mM NaCl, 3mM EDTA, 0.0% Tween-20) at 25degC. Six-point antigen dilution series were prepared  
558 in running buffer starting at 200 nM with a 2.5-fold serial dilution (200-2.0nM). Antibodies were first  
559 captured on a Carterra HC30M sensor chip with immobilized goat anti-human Fc pAb. Following 8-10  
560 buffer injection cycles, increasing antigen concentrations were injected over the Ab-captured surfaces with a  
561 5 min of association phase and a 10 min of dissociation phase. The chip surface was finally regenerated  
562 and antibodies were recaptured for subsequent antigen binding studies. Double reference subtracted data  
563 containing antigen binding at varying concentrations were globally fit using 1:1 binding model. Binding  
564 affinity measurements and analyses were performed by Twist Bioscience.

## 565 References

1. Andrew Leaver-Fay, Michael Tyka, Steven M Lewis, Oliver F Lange, James Thompson, Ron Jacak, Kristian W Kaufman, P Douglas Renfrew, Colin A Smith, Will Sheffler, et al. Rosetta3: an object-oriented software suite for the simulation and design of macromolecules. In *Methods in enzymology*, volume 487, pages 545–574. Elsevier, 2011.
2. John Ingraham, Vikas Garg, Regina Barzilay, and Tommi Jaakkola. Generative models for graph-based protein design. *Advances in neural information processing systems*, 32, 2019.
3. Justas Dauparas, Ivan Anishchenko, Nathaniel Bennett, Hua Bai, Robert J Ragotte, Lukas F Miles, Basile IM Wicky, Alexis Courbet, Rob J de Haas, Neville Bethel, et al. Robust deep learning-based protein sequence design using proteinmpnn. *Science*, 378(6615):49–56, 2022.
4. Chloe Hsu, Robert Verkuil, Jason Liu, Zeming Lin, Brian Hie, Tom Sercu, Adam Lerer, and Alexander Rives. Learning inverse folding from millions of predicted structures. In *International Conference on Machine Learning*, pages 8946–8970. PMLR, 2022.
5. BIM Wicky, LF Miles, A Courbet, RJ Ragotte, J Dauparas, E Kinfu, S Tipps, RD Kibler, M Baek, F DiMaio, et al. Hallucinating symmetric protein assemblies. *Science*, 378(6615):56–61, 2022.
6. Kiera H Sumida, Reyes Núñez-Franco, Indrek Kalvet, Samuel J Pellock, Basile IM Wicky, Lukas F Miles, Justas Dauparas, Jue Wang, Yakov Kipnis, Noel Jameson, et al. Improving protein expression, stability, and function with proteinmpnn. *Journal of the American Chemical Society*, 146(3):2054–2061, 2024.
7. Florian Praetorius, Philip JY Leung, Maxx H Tessmer, Adam Broerman, Cullen Demakis, Acacia F Dishman, Arvind Pillai, Abbas Idris, David Juergens, Justas Dauparas, et al. Design of stimulus-responsive two-state hinge proteins. *bioRxiv*, pages 2023–01, 2023.
8. Helen M Berman, John Westbrook, Zukang Feng, Gary Gilliland, Talapady N Bhat, Helge Weissenig, Ilya N Shindyalov, and Philip E Bourne. The protein data bank. *Nucleic acids research*, 28(1):235–242, 2000.
9. John Jumper, Richard Evans, Alexander Pritzel, Tim Green, Michael Figurnov, Olaf Ronneberger, Kathryn Tunyasuvunakool, Russ Bates, Augustin Žídek, Anna Potapenko, et al. Highly accurate protein structure prediction with alphafold. *Nature*, 596(7873):583–589, 2021.
10. Roshan Rao, Joshua Meier, Tom Sercu, Sergey Ovchinnikov, and Alexander Rives. Transformer protein language models are unsupervised structure learners. In *International Conference on Learning Representations*, 2020.
11. Zeming Lin, Halil Akin, Roshan Rao, Brian Hie, Zhongkai Zhu, Wenting Lu, Nikita Smetanin, Robert Verkuil, Ori Kabeli, Yaniv Shmueli, et al. Evolutionary-scale prediction of atomic-level protein structure with a language model. *Science*, 379(6637):1123–1130, 2023.
12. Daniel Hesslow, Niccolò Zanichelli, Pascal Notin, Iacopo Poli, and Debora Marks. Rita: a study on scaling up generative protein sequence models. *arXiv preprint arXiv:2205.07589*, 2022.
13. Erik Nijkamp, Jeffrey A Ruffolo, Eli N Weinstein, Nikhil Naik, and Ali Madani. Progen2: exploring the boundaries of protein language models. *Cell Systems*, 2023.
14. Ali Madani, Ben Krause, Eric R Greene, Subu Subramanian, Benjamin P Mohr, James M Holton, Jose Luis Olmos Jr, Caiming Xiong, Zachary Z Sun, Richard Socher, et al. Large language models generate functional protein sequences across diverse families. *Nature Biotechnology*, pages 1–8, 2023.
15. Geraldene Munsamy, Ramiro Illanes-Vicioso, Silvia Funcillo, Ioanna T Nakou, Sebastian Lindner, Gavin Ayres, Lesley S Sheehan, Steven Moss, Ulrich Eckhard, Philipp Lorenz, et al. Conditional language models enable the efficient design of proficient enzymes. *bioRxiv*, pages 2024–05, 2024.
16. Jeffrey A Ruffolo, Stephen Nayfach, Joseph Gallagher, Aadyot Bhatnagar, Joel Beazer, Riffat Hussain, Jordan Russ, Jennifer Yip, Emily Hill, Martin Pacesa, et al. Design of highly functional genome editors by modeling the universe of crisper-cas sequences. *bioRxiv*, pages 2024–04, 2024.
17. Jonas Pfeiffer, Aishwarya Kamath, Andreas Rücklé, Kyunghyun Cho, and Iryna Gurevych. Adapterfusion: Non-destructive task composition for transfer learning. *arXiv preprint arXiv:2005.00247*, 2020.
18. Neil Houlsby, Andrei Giurgiu, Stanislaw Jastrzebski, Bruna Morrone, Quentin De Laroussilhe, Andrea Gesmundo, Mona Attariyan, and Sylvain Gelly. Parameter-efficient transfer learning for nlp. In *International Conference on Machine Learning*, pages 2790–2799. PMLR, 2019.
19. Edward J Hu, Yelong Shen, Philip Wallis, Zeyuan Allen-Zhu, Yuanzhi Li, Shean Wang, Lu Wang, and Weizhu Chen. Lora: Low-rank adaptation of large language models. *arXiv preprint arXiv:2106.09685*, 2021.
20. Nicholas Z Randolph and Brian Kuhlman. Invariant point message passing for protein side chain packing. *Proteins: Structure, Function, and Bioinformatics*, 2024.
21. Christine A Orengo, Alex D Michie, Susan Jones, David T Jones, Mark B Swindells, and Janet M Thornton. Cath—a hierachic classification of protein domain structures. *Structure*, 5(8):1093–1109, 1997.
22. Zhangyang Gao, Cheng Tan, and Stan Z Li. Pifold: Toward effective and efficient protein inverse folding. In *The Eleventh International Conference on Learning Representations*, 2022.

- 603 23. Justas Dauparas, Gyu Rie Lee, Robert Pecoraro, Linna An, Ivan Anishchenko, Cameron Glasscock, and David Baker. Atomic context-conditioned protein sequence design using ligandmpnn. *BioRxiv*,  
604 pages 2023–12, 2023.
- 605 24. Lucien Krapp, Fernando Meireles, Luciano Abriata, and Matteo Dal Peraro. Context-aware geometric deep learning for protein sequence design. *BioRxiv*, pages 2023–06, 2023.
- 606 25. Pascal Notin, Aaron W Kollasch, Daniel Ritter, Lood van Niekerk, Steffanie Paul, Hansen Spinner, Nathan Rollins, Ada Shaw, Ruben Weitzman, Jonathan Frazer, et al. Proteingym: Large-scale  
607 benchmarks for protein design and fitness prediction. *BioRxiv*, pages 2023–12, 2023.
- 608 26. Nicole M Gaudelli, Alexis C Komor, Holly A Rees, Michael S Packer, Ahmed H Badran, David I Bryson, and David R Liu. Programmable base editing of a•t to g•c in genomic dna without dna  
609 cleavage. *Nature*, 551(7681):464–471, 2017.
- 610 27. Nicole M Gaudelli, Dieter K Lam, Holly A Rees, Noris M Solá-Esteves, Luis A Barrera, David A Born, Aaron Edwards, Jason M Gehrke, Seung-Joo Lee, Alexander J Liquori, et al. Directed evolution of  
611 adenine base editors with increased activity and therapeutic application. *Nature biotechnology*, 38(7):892–900, 2020.
- 612 28. Audrone Lapinaite, Gavin J Knott, Cody M Palumbo, Enrique Lin-Shiao, Michelle F Richter, Kevin T Zhao, Peter A Beal, David R Liu, and Jennifer A Doudna. Dna capture by a crispr-cas9–guided  
613 adenine base editor. *Science*, 369(6503):566–571, 2020.
- 614 29. Brian L Hie, Varun R Shanker, Duo Xu, Theodora UJ Bruun, Payton A Weidenbacher, Shaogeng Tang, Wesley Wu, John E Pak, and Peter S Kim. Efficient evolution of human antibodies from general  
615 protein language models. *Nature Biotechnology*, 2023.
- 616 30. David Prihoda, Jad Maamary, Andrew Waight, Veronica Juan, Laurence Fayadat-Dilman, Daniel Svozil, and Danny A Bitton. Biophi: a platform for antibody design, humanization, and humanness  
617 evaluation based on natural antibody repertoires and deep learning. In *MAbs*, volume 14, page 2020203. Taylor & Francis, 2022.
- 618 31. James Dunbar, Konrad Krawczyk, Jinwoo Leem, Terry Baker, Angelika Fuchs, Guy Georges, Jiye Shi, and Charlotte M Deane. Sabdab: the structural antibody database. *Nucleic acids research*, 42  
619 (D1):D1140–D1146, 2014.
- 620 32. Richard W Shuai, Jeffrey A Ruffolo, and Jeffrey J Gray. IgLM: Infilling language modeling for antibody sequence design. *Cell Systems*, 14(11):979–989, 2023.
- 621 33. Mark Hutchinson, Jeffrey A Ruffolo, Nantaporn Haskins, Michael Iannotti, Giuliana Vozza, Tony Pham, Nurjahan Mehzabeen, Harini Shandilya, Keith Rickert, Rebecca Croasdale-Wood, et al. Toward  
622 enhancement of antibody thermostability and affinity by computational design in the absence of antigen. *mAbs*, 16(1):2362775, 2024.
- 623 34. Yeqing Lin, Minji Lee, Zhao Zhang, and Mohammed AlQuraishi. Out of many, one: Designing and scaffolding proteins at the scale of the structural universe with genie 2. *arXiv preprint arXiv:2405.15489*,  
624 2024.
- 625 35. Deniz Akpinaroglu, Kosuke Seki, Amy Guo, Eleanor Zhu, Mark JS Kelly, and Tanja Kortemme. Structure-conditioned masked language models for protein sequence design generalize beyond the  
626 native sequence space. *BioRxiv*, pages 2023–12, 2023.
- 627 36. Martin Steinegger and Johannes Söding. Clustering huge protein sequence sets in linear time. *Nature communications*, 9(1):1–8, 2018.
- 628 37. Diederik P Kingma and Jimmy Ba. Adam: A method for stochastic optimization. *arXiv preprint arXiv:1412.6980*, 2014.
- 629 38. Zaixiang Zheng, Yifan Deng, Dongyu Xue, Yi Zhou, Fei Ye, and Quanquan Gu. Structure-informed language models are protein designers. *BioRxiv*, pages 2023–02, 2023.
- 630 39. Jeffrey M Spencer and Xiaoliu Zhang. Deep mutational scanning of *s. pyogenes* cas9 reveals important functional domains. *Scientific reports*, 7(1):16836, 2017.
- 631 40. Li Xu, Yakun Liu, and Renzhi Han. Beat: a python program to quantify base editing from sanger sequencing. *The CRISPR journal*, 2(4):223–229, 2019.
- 632 41. David Conant, Tim Hsiao, Nicholas Rossi, Jennifer Oki, Travis Maures, Kelsey Waite, Joyce Yang, Sahil Joshi, Reed Kelso, Kevin Holden, et al. Inference of crispr edits from sanger trace data. *The  
633 CRISPR journal*, 5(1):123–130, 2022.
- 634 42. Bowen Jing, Stephan Eismann, Patricia Suriana, Raphael John Lamarre Townshend, and Ron Dror. Learning from protein structure with geometric vector perceptrons. In *International Conference on  
635 Learning Representations*, 2020.

636 **Supplementary information**

**Table S1. CATH 4.2 benchmark.** Comparison of recent protein design models on the CATH 4.2 test set from (2). Perplexity is reported over all residues in the test set. † indicates results cited from (22). ‡ indicates results cited from (38).

Model	Train / Total Param.	Perplexity (↓)	Median Recovery (%), ↑
†Structured Transformer (2)	1.6M / 1.6M	6.63	35.82
†GVP-GNN (42)	1.0M / 1.0M	5.36	39.47
†ProteinMPNN (3)	1.9M / 1.9M	4.61	45.96
†PiFold (22)	6.6M / 6.6M	4.55	51.66
‡ProteinMPNN-CMLM (38)	1.9M / 1.9M	5.03	48.62
‡LM-Design (ProteinMPNN-CMLM) (38)	6.9M / 659M (1.0%)	4.63	53.26
‡LM-Design (PiFold) (38)	11.9M / 664M (1.7%)	4.52	55.65
Causal encoder	4.1M / 4.1M	4.76	47.24
proseLM-S	5.1M / 156M (3.3%)	3.89	49.00
proseLM-Base	7.3M / 772M (0.9%)	3.34	49.6
proseLM-M	7.3M / 772M (0.9%)	3.29	50.00
proseLM-L	10.8M / 2.8B (0.4%)	3.23	50.34
proseLM-XL	13.3M / 6.5B (0.2%)	2.67	50.83

**Table S2. PDB benchmark.** Comparison of proseLM models on PDB test set derived from (3). Metrics are for proteins that are part of a complex or have interactions with some non-protein entity. Performance is reported for both backbone-only and full-context inputs (backbone / full). For protein complexes, all other chains are provided as context for the target chain.

Model	Train / Total Param.	Mean Perplexity (↓)	Median Recovery (%), ↑
Causal encoder	4.2M / 4.2M	4.17 / 3.64	54.36 / 58.15
proseLM-S	988K / 155M (0.6%)	3.77 / 3.34	55.63 / 59.57
proseLM-M	3.2M / 772M (0.4%)	3.32 / 3.00	57.00 / 61.20
proseLM-L	6.6M / 2.8B (0.2%)	3.39 / 3.05	56.89 / 61.53
proseLM-XL	9.2M / 6.5B (0.1%)	2.80 / 2.57	59.58 / 64.41

**Table S3. Sequence recovery near non-protein context.** Comparison of proseLM models on PDB test set derived from (3). Metrics are for residues within 5 Å of nucleic acids, ligands, or ions. Performance is reported for both backbone-only and full-context inputs (backbone / full).

Model	Median Recovery (%), ↑		
	Nucleic Acid	Ligand	Ion
Causal encoder	44.44 / 54.90	50.00 / 64.00	46.15 / 66.67
proseLM-S	48.94 / 58.06	57.14 / 70.59	60.00 / 76.00
proseLM-M	64.24 / 70.87	66.67 / 75.93	70.97 / 82.61
proseLM-L	62.88 / 71.13	66.67 / 76.47	70.59 / 82.61
proseLM-XL	70.59 / 76.10	74.19 / 82.35	77.78 / 87.50

**Table S4. SAbDab antibody benchmark.** Comparison of proseLM models on antibody test set from SAbDab. Sequence recovery is reported as the median of cluster-averaged values for all antigen-bound heavy (n = 361) and light (n = 300) chains in the test set. Performance is reported for both antibody-only and full-complex inputs (antibody / complex).

Model	Median Recovery (%), ↑	
	Heavy Fv	Light Fv
Causal encoder	75.90 / 77.37	75.68 / 77.48
proseLM-S	78.56 / 78.94	77.57 / 78.06
proseLM-M	79.91 / 79.96	79.61 / 79.44
proseLM-L	80.71 / 82.04	82.14 / 83.17
proseLM-XL	80.60 / 81.57	80.09 / 81.02
proseLM-Ab	79.80 / 82.42	83.11 / 83.02

**Table S5. SAbDab bound antibody benchmark.** Comparison of proseLM models on antibody test set from SAbDab. Sequence recovery is reported as the median of cluster-averaged values for all antigen-bound heavy (n = 361) and light (n = 300) chains in the test set. Performance is reported for both antibody-only and full-complex inputs (antibody / complex). CDR loops are defined according to the IMGT numbering scheme.

Model	Median Recovery (%), ↑							
	Heavy Fr	CDR H1	CDR H2	CDR H3	Light Fr	CDR L1	CDR L2	CDR L3
Causal encoder	83.23 / 82.73	67.22 / 69.23	55.56 / 60.00	50.00 / 60.00	81.01 / 82.28	65.00 / 66.67	62.50 / 62.50	56.25 / 59.09
proseLM-S	85.42 / 84.70	69.23 / 72.48	60.00 / 63.65	52.51 / 57.70	82.28 / 82.28	63.64 / 66.20	62.50 / 68.75	56.36 / 60.42
proseLM-M	87.50 / 87.57	69.23 / 69.23	60.00 / 62.60	52.66 / 58.82	84.81 / 84.21	66.67 / 66.67	66.67 / 75.00	57.78 / 60.00
proseLM-L	88.62 / 88.10	69.41 / 74.03	60.00 / 66.67	52.63 / 62.83	86.00 / 86.08	68.18 / 68.18	75.00 / 75.00	65.08 / 66.67
proseLM-XL	88.39 / 88.11	69.23 / 70.19	60.00 / 68.93	50.00 / 60.56	84.54 / 85.53	69.23 / 71.10	71.43 / 75.00	59.26 / 62.50
proseLM-Ab	89.09 / 89.70	69.23 / 71.43	59.44 / 63.33	50.00 / 60.41	86.71 / 86.71	66.67 / 72.73	75.00 / 75.00	62.50 / 66.67

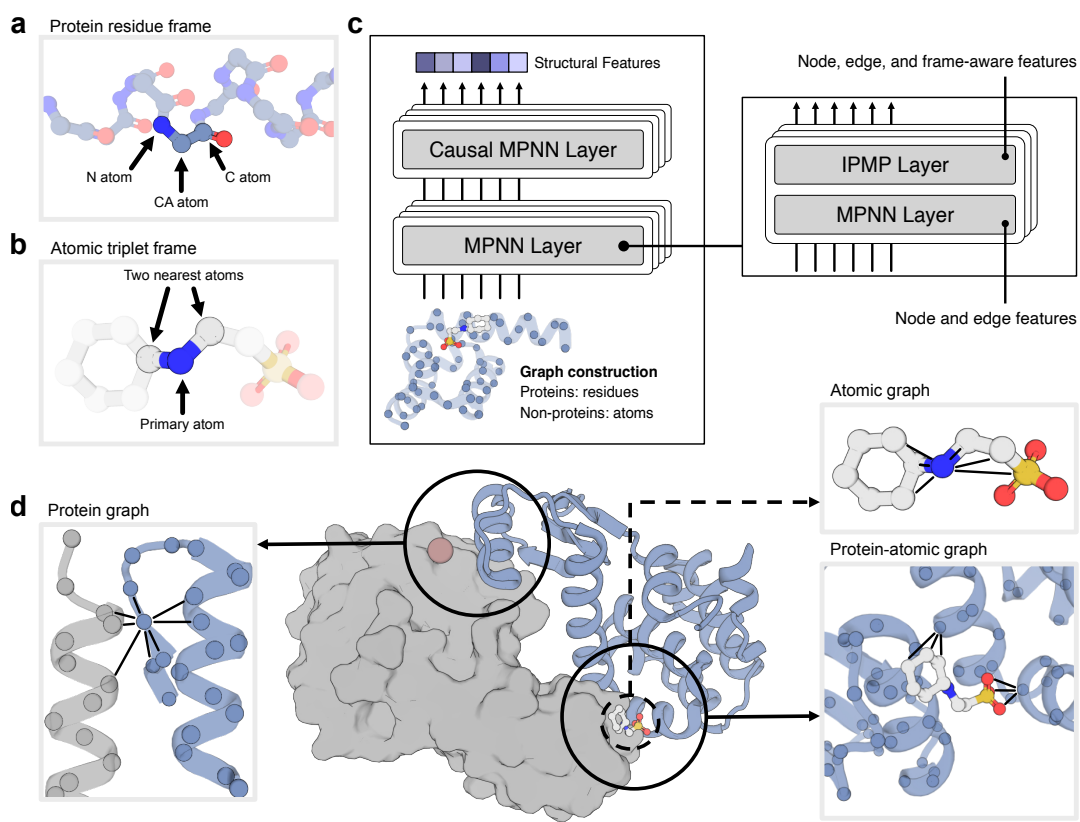


**Fig. S1. Visualization of protein and atomic graph components.** (a) Each protein residue is represented as a rigid body frame with the  $C_{\alpha}$  atom at the origin and the frame's orientation defined by the positions of the N and C atoms. (b) Non-protein atoms are represented as rigid body frames with the primary atom at the origin and the two closest atoms defining the frame's orientation. (c) Protein and atomic graphs are processed by alternating MPNN and IPMP (20) layers. MPNN layers operate on the graph nodes and edges, while IPMP layers additionally incorporate frame-based geometric features. (d) Visualization of the edge connectivity for the protein-only residue graph (left), atomic-only graph (upper right), and protein-atomic graph (lower right). Black lines illustrate the connectivity between nodes in the graph.

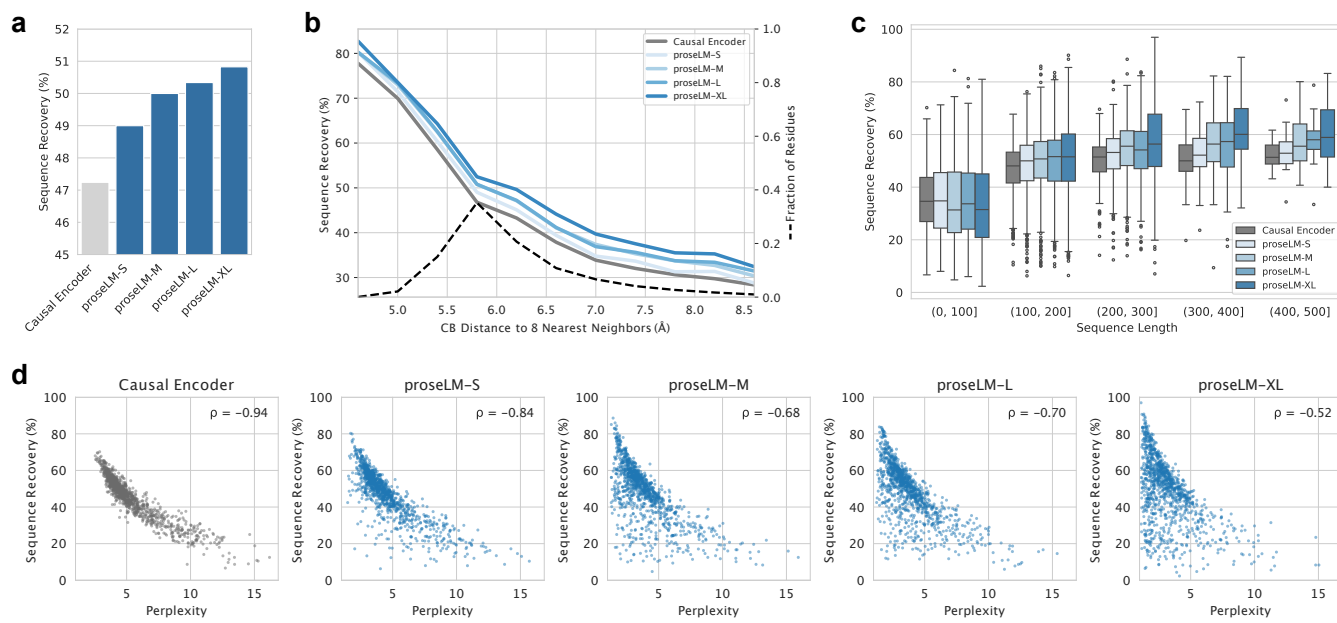


**Fig. S2. Performance of proseLM models on CATH 4.2 benchmark.** Evaluation of proseLM model performance on the CATH 4.2 test set curated by Ingraham et al. (2). Aggregate sequence recovery values are reported as the median across all proteins (or subsets when appropriate). (a) Recovery of native sequence residues for proseLM models. (b) Recovery of native sequence residues for proseLM models binned by residue burial, calculated as the average  $C_\beta$  distance to the nearest eight neighbors (lower is more buried). All models achieve highest rates of native sequence recovery among buried residues and reduced recovery at less-buried surface positions. (c) Recovery of native sequence residues for proseLM models, binned by sequence length. Longer sequences exhibit higher rates of native sequence recovery, with larger proseLM models having particularly high recovery for large proteins. (d) Relationship between perplexity and sequence recovery for proseLM models. Spearman correlation coefficients are reported for each model. Larger models show less correlation between perplexity and sequence recovery.

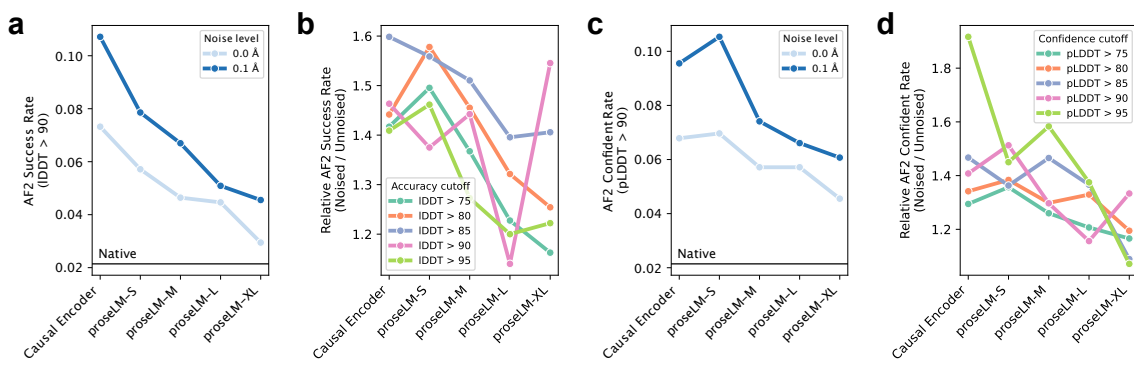


**Fig. S3. Impact of coordinate noise on single-sequence structure prediction.** Evaluation of proselM model performance on the CATH 4.2 test set with and without Gaussian noise added to coordinates. Structure prediction accuracy and confidence are for single-sequence predictions using AlphaFold2 (9). (a) Fraction of designed sequences that are predicted to successfully recapitulate the input structure (IDDT > 90). Models trained with 0.1 Å of Gaussian noise added to coordinates achieve higher structure prediction success. Larger models approach the lower level of structure prediction success of the native sequences (Horizontal line) (b) Structure prediction success rates for noised models relative to un-noised for several IDDT thresholds. Larger models show less sensitivity to coordinate noise (lower relative success rates). (c) Fraction of designed sequences that yield highly confident structure predictions (pLDDT > 90). Models trained with coordinate noise yield high-confidence structures more frequently. Larger models approach the lower level of confident structure prediction rates for the native sequences (Horizontal line). (d) Confidence in structure prediction for noised models relative to un-noised for several pLDDT thresholds. Larger models show less sensitivity to coordinate noise (lower relative rates of confident predictions).

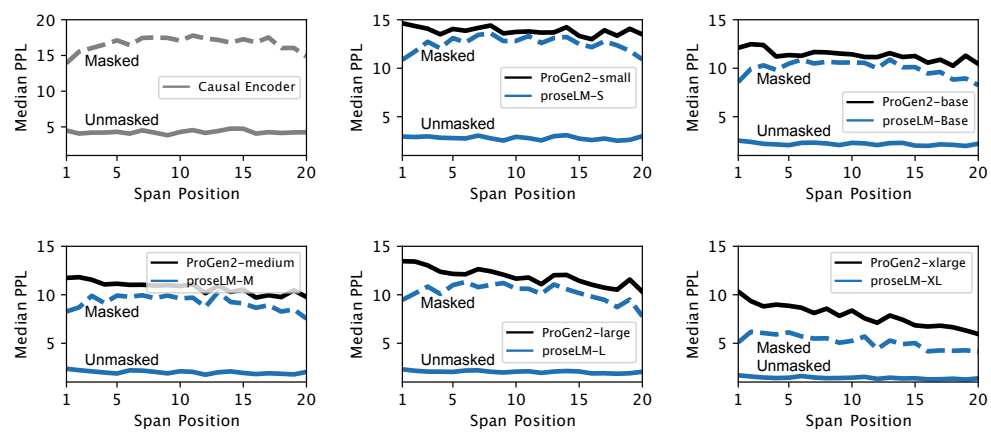


**Fig. S4. Perplexity of masked structural spans.** Evaluation of proseLM model perplexity on contiguous structurally masked spans of twenty residues. Perplexity for structurally masked residues (dashed lines) increases significantly over the same residues without masking (solid lines). Compared to the respective ProGen2 models, proseLM models achieve lower perplexity for structurally masked residues, indicating that the surrounding context is effectively incorporated when predicting for masked positions.

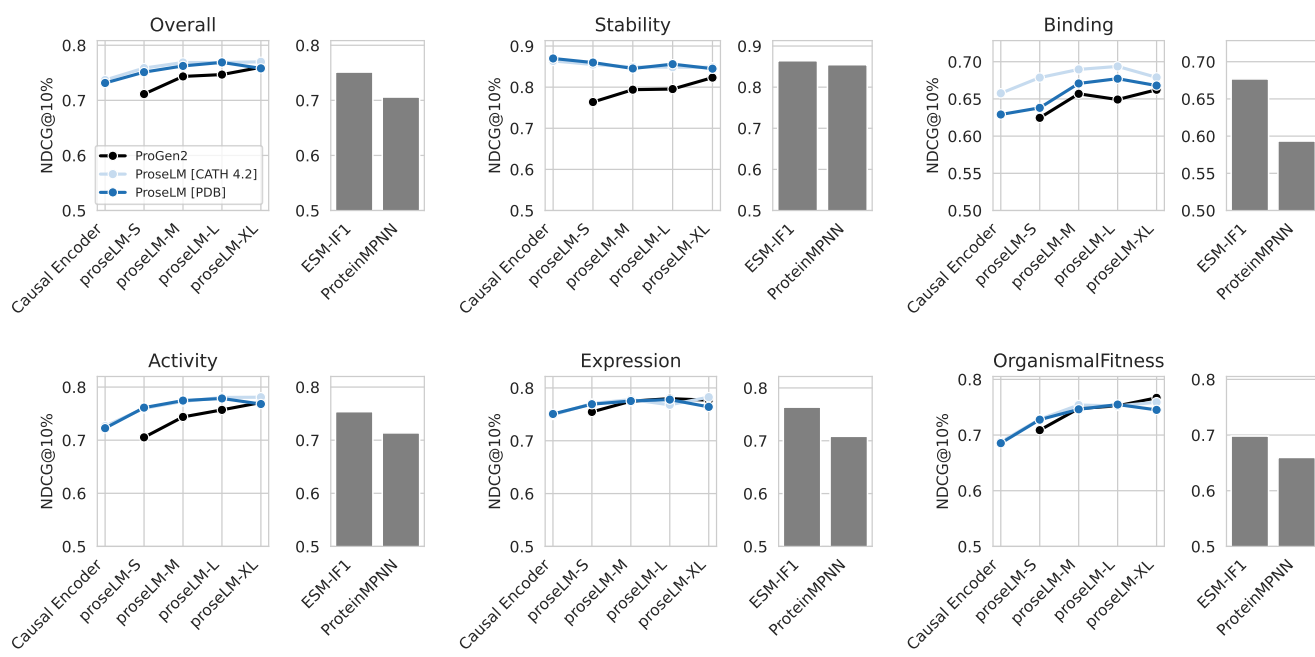


**Fig. S5. Fitness prediction measured by normalized discounted cumulative gain.** Comparison of proseLM and recent structure-conditioned sequence design models (ESM-IF1 and ProteinMPNN) for prediction of mutational fitness landscapes. Performance is reported as normalized discounted cumulative gain for the top ten percent of samples according to experimental fitness (NDCG10%). The metric is relevant for protein design tasks, where it is important to accurately prioritize the highest fitness sequences for experimental characterization.

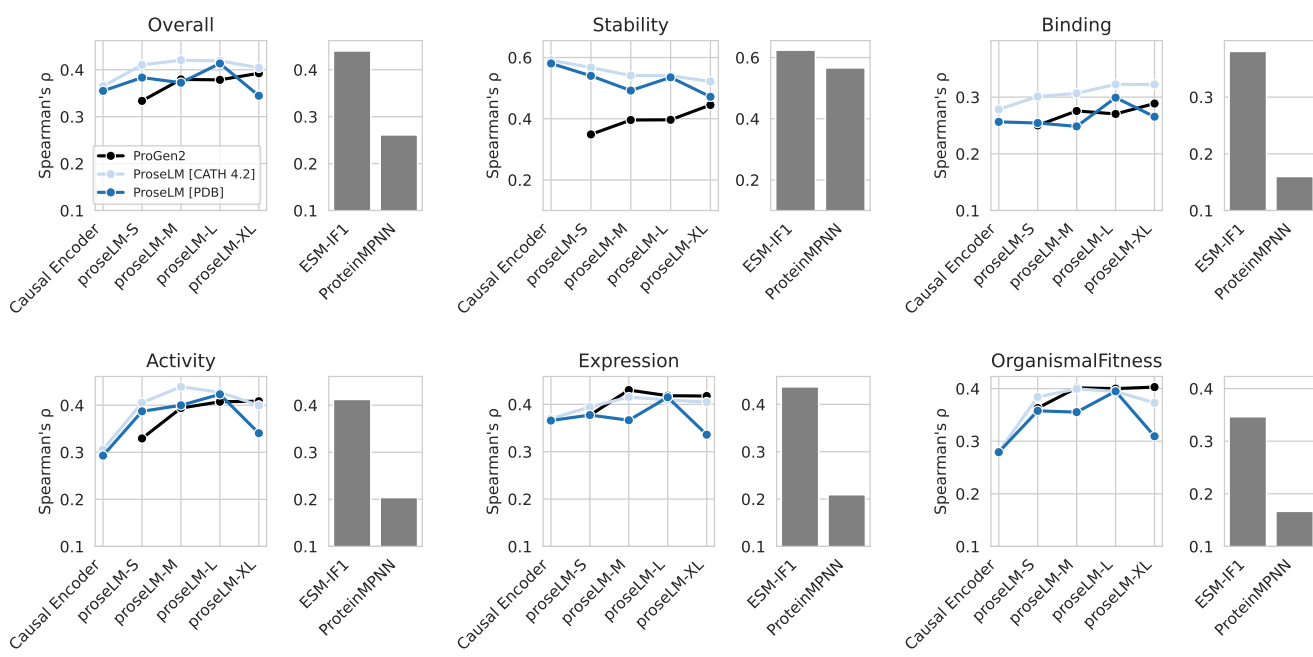


**Fig. S6. Fitness prediction measured by Spearman's rank correlation coefficient.** Comparison of proseLM and recent structure-conditioned sequence design models (ESM-IF1 and ProteinMPNN) for prediction of mutational fitness landscapes. Performance is reported as Spearman's rank correlation coefficients. The metric indicates how well model scores rank sequences according to fitness across the entire dataset.

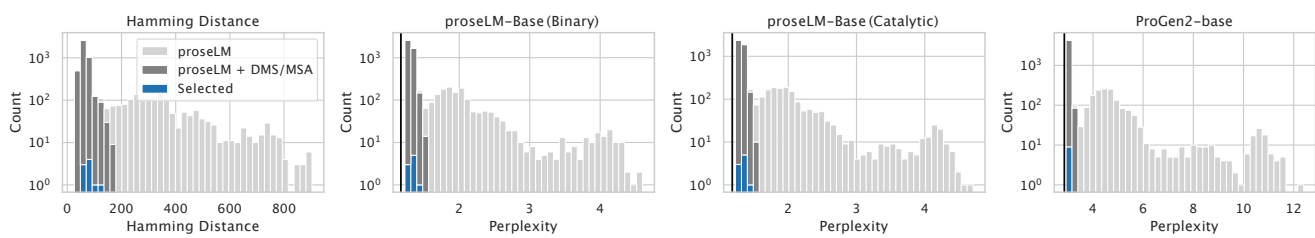


**Fig. S7. Model scores for SpCas9 variants.** Mutational hamming distance from SpCas9 and proseLM model perplexities for designed SpCas9 variants. Mutation distances and model scores are shown for generations directly from proseLM (light gray), generations from proseLM augmented with position-specific residue propensities from deep mutational scans and multiple-sequence alignments (dark gray), and the subset selected for experimental validation (blue). Model scores for SpCas9 are indicated by vertical black lines.

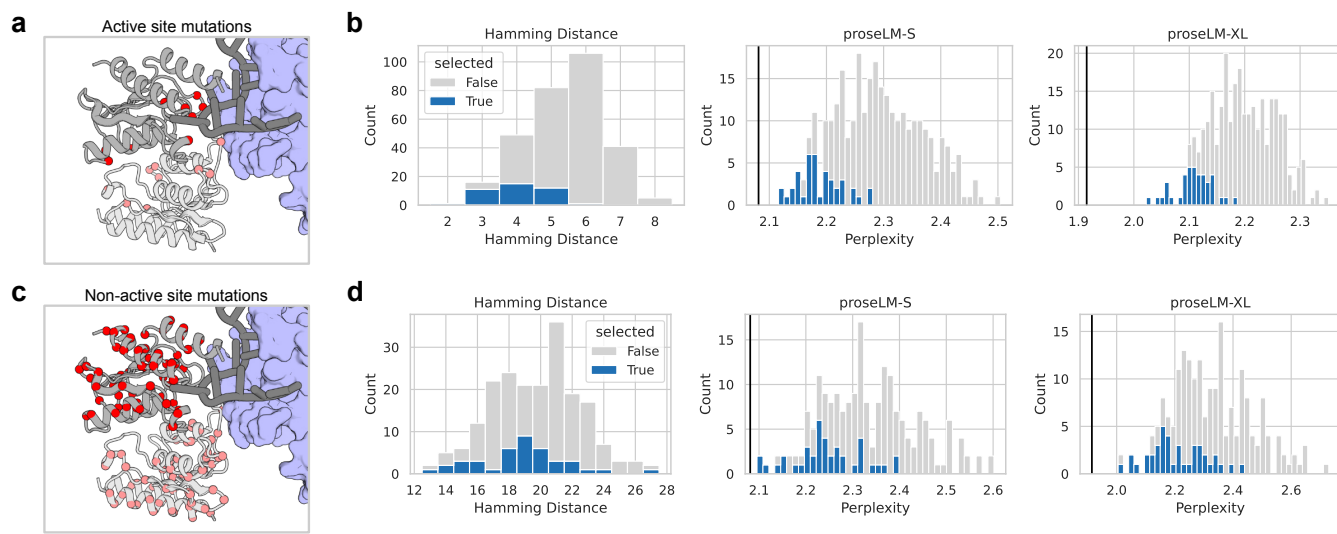


**Fig. S8. Model scores for adenine base editor variants.** Mutational hamming distance from parental deaminase and proseLM model perplexities for designed deaminase variants. Mutation distances and model scores for the complete set of generations and the subset selected for experimental validation are shown in gray and blue, respectively. Model scores for the parental deaminase are indicated by vertical black lines. (a) Positions of all mutated residues among selected active site variants (red spheres). (b) Mutation and score distributions for active site variants. (c) Positions of all mutated residues among selected non-active site variants (red spheres). (d) Mutation and score distributions for non-active site variants.

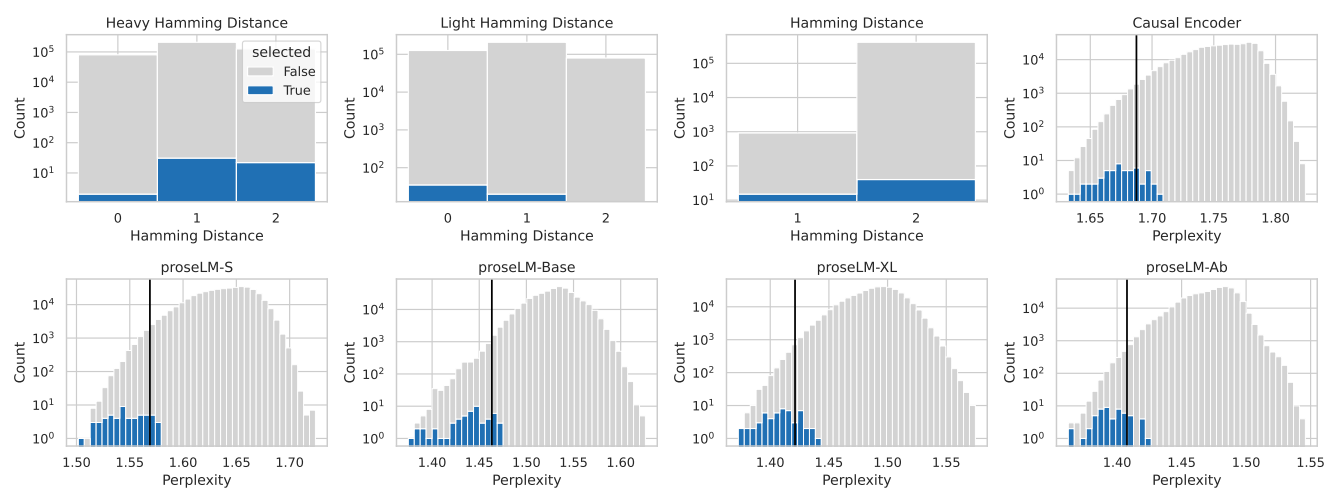


**Fig. S9. Model scores for nivolumab CDR variants.** Mutational hamming distance from parental nivolumab and proseLM model perplexities for designed nivolumab CDR loop variants. Mutation distances and model scores for the complete set of generations and the subset selected for experimental validation are shown in gray and blue, respectively. Model scores for nivolumab are indicated by vertical black lines. Y-axis is shown on a log scale.

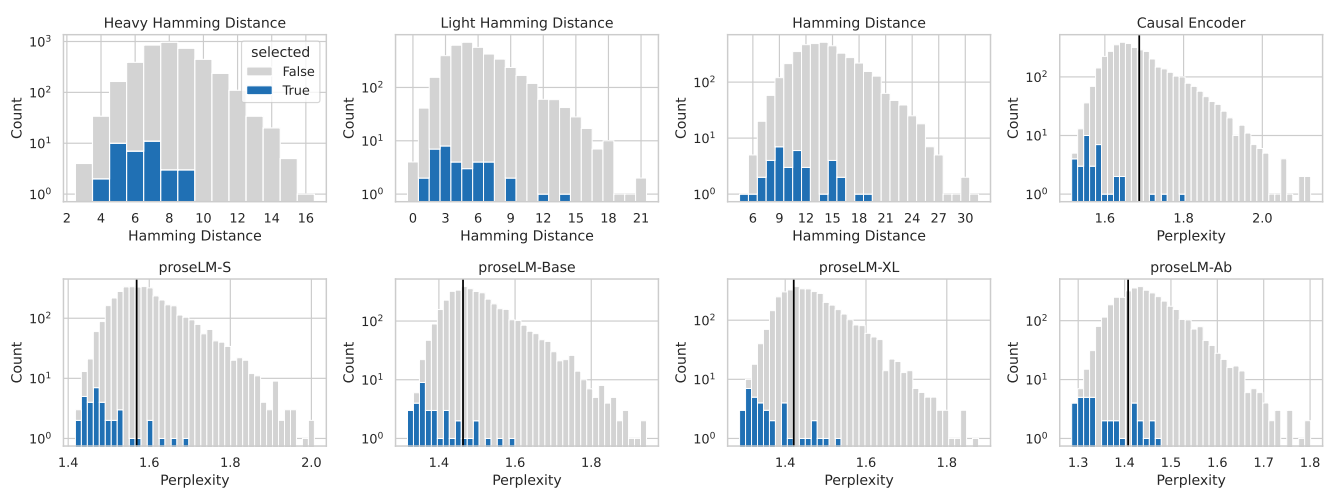


**Fig. S10. Model scores for nivolumab framework variants.** Mutational hamming distance from parental nivolumab and proselM model perplexities for designed nivolumab framework variants. Mutation distances and model scores for the complete set of generations and the subset selected for experimental validation are shown in gray and blue, respectively. Model scores for nivolumab are indicated by vertical black lines. Y-axis is shown on a log scale.

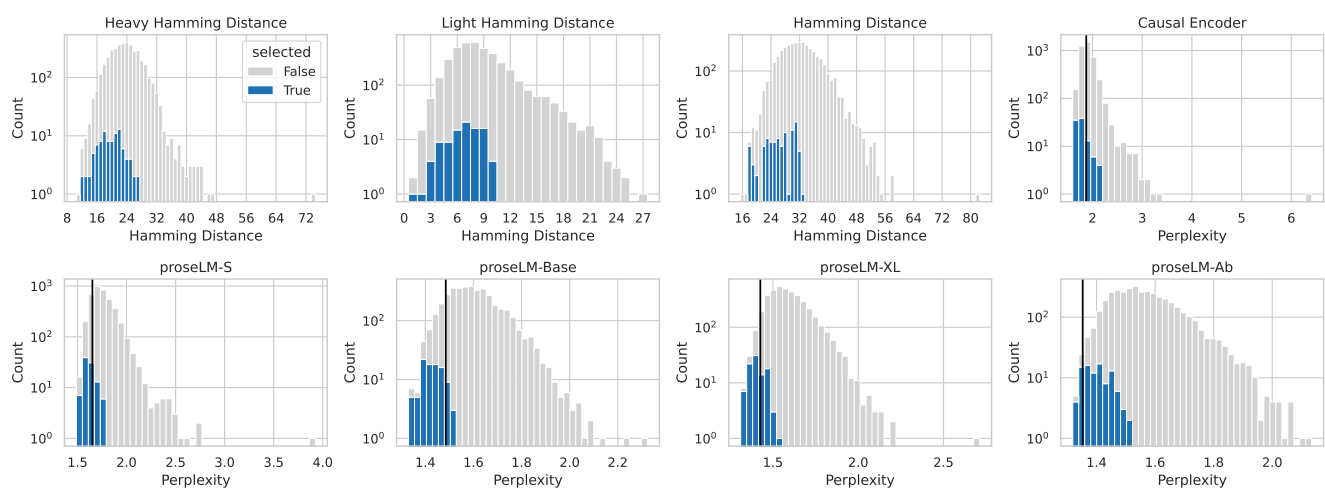


**Fig. S11. Model scores for diversified secukinumab variants.** Mutational hamming distance from parental secukinumab and proseLM model perplexities for designed secukinumab variants. Mutation distances and model scores for the complete set of generations and the subset selected for experimental validation are shown in gray and blue, respectively. Model scores for secukinumab are indicated by vertical black lines. Y-axis is shown on a log scale.